Icarus 251 (2015) 226–243

Contents lists available at ScienceDirect

Icarus

journal homepage: www.elsevier.com/locate/icarus

Present-day seasonal gully activity in a south polar pit (Sisyphi Cavi) on Mars

J. Raack [a,*], D. Reiss [a], T. Appéré [b], M. Vincendon [c], O. Ruesch [a], H. Hiesinger [a]

[a] Institut für Planetologie, Westfälische Wilhelms-Universität Münster, Wilhelm-Klemm-Str. 10, 48149 Münster, Germany
[b] Laboratoire AIM, CEA-Saclay, DSM/IRFU/SAp, 91191 Gif-sur-Yvette, France
[c] Institut d'Astrophysique Spatiale, Université Paris Sud, 91400 Orsay, France

ARTICLE INFO

Article history:
Received 8 November 2013
Revised 5 March 2014
Accepted 25 March 2014
Available online 5 April 2014

Keywords:
Mars, polar geology
Mars, climate
Mars, surface
Photometry
Spectroscopy

ABSTRACT

The large amount of multi-temporal high-resolution images acquired in the last few years offers the opportunity to identify morphological changes associated with recent geologic activity on the surface of Mars. In this study we focus on a single gully in Sisyphi Cavi, located in the south polar region at 1.44°E and 68.54°S. The gully incises the gullied equator-facing slope of an isolated polar pit within an infilled impact crater. It is important to notice that the following investigations describe the activity and modifications of an existing gully and not the formation of the gully itself. High-resolution image data analyses show new deposits at the terminus of the gully channel and on the gully apron within spring (after solar longitudes of 236°) of martian years (MY) 29 and 31. Our morphological investigations show that the identified new deposits were formed by dark flows through the entire gully deposited on top of the apron between solar longitudes (L_S) ~218° and ~226°. Thermal data show a temperature increase between L_S ~218° and ~226°. Near-infrared spectral data show relatively constant band strengths of CO_2 ice and H_2O ice in this time range. After the formation of the dark flows (after L_S ~226°), temperatures increase rapidly from ~180 K to >~270 K at L_S ~250°. At this time, spectral data indicate that all volatiles on the surface sublimated. However, an earlier beginning of sublimation when the dark flows were observed (between L_S ~218° and ~226°) is likely, due to the fact that the instruments can only show the last phase of sublimation (decrease of volatile band strengths). Spectral modeling shows that from winter to mid-spring, the surface of the studied area is covered by translucent CO_2 slab-ice contaminated by minor amounts of H_2O ice and dust. Furthermore, our spectral modeling indicates that the dark material most likely flows on top of the CO_2 slab-ice cover. Three different scenarios were proposed to explain the identified dark flows, including (1) flows supported by liquid H_2O, (2) flows supported by CO_2 gas, and (3) dry flows. On the basis of our study we find that scenario (1) is unlikely because of the very low temperatures. While scenario (2) is consistent with the observed beginning of CO_2 ice sublimation in the study area, it is unlikely because of the limitation of the activity to only one gully compared to surrounding gullies that share the same morphologies, slope angles, and volatile contents. Also with scenario (3), dry flows, the activity of only one gully is difficult to explain. Thus, we propose a mixture of scenario (2 and 3), dry flows supported by the ongoing sublimation of CO_2 ice within the gully, to be the most plausible scenario, when the observed active gully comprises different source material than the surrounding gullies, i.e., a higher content of probably sand-sized material from outcrops located in the alcove.

1. Introduction

Gullies on Mars were first detected by Malin and Edgett (2000) in high-resolution Mars Orbiter Camera-Near Angle (MOC-NA) imagery. In this work, gullies showing the typical morphology of an alcove, channel, and apron (Malin and Edgett, 2000) are described by the term "classical gullies". Classical gullies might be formed by subsurface water release (e.g., Malin and Edgett, 2000), CO_2-based liquid or gas supported flows (e.g., Musselwhite et al., 2001), melting of near-surface H_2O ice (e.g., Costard et al., 2002; Reiss et al., 2009; Jouannic et al., 2012) or surface snow (Christensen, 2003; Head et al., 2008), or by dry granular flows (Treiman, 2003; Shinbrot et al., 2004).

* Corresponding author.
E-mail address: jan.raack@uni-muenster.de (J. Raack).

http://dx.doi.org/10.1016/j.icarus.2014.03.040
0019-1035/

The global distribution of gullies is limited to mid- and high-latitudes poleward of ~30° in both hemispheres with an orientation of gullies on mostly poleward-facing slopes (e.g., Malin and Edgett, 2000; Balme et al., 2006) shifting to a predominantly equatorward orientation between ~44°S and 64°S (e.g., Heldmann and Mellon, 2004; Aston et al., 2011; Raack et al., 2012a). In the northern hemisphere, Heldmann et al. (2007) and Kneissl et al. (2010) observed a predominantly equatorward orientation of gullies. The strong latitude-dependence of gullies and their assemblage with viscous flow features and the dust–ice mantle (Milliken et al., 2003) suggest a climatic influence on their formation, possibly caused by obliquity changes in the recent past (Head et al., 2003). Hoffman (2002) investigated gullies in the southern polar region (Sisyphi Cavi), adjacent to our study region. He estimated that gullies within Sisyphi Cavi are young (~20 ka to ~20 Ma) and were formed in spring by CO_2-gas lubricated flows.

Dickson and Head (2009) estimated that gullies were active in the last several millions of years (Ma) by an episodic melting of an atmospherically emplaced snow/ice cover during spin-axis orbital variations of Mars. Investigations by Reiss et al. (2004) and Schon et al. (2009) show gully ages of less than ~3 Ma and ~1.25 Ma, respectively. Raack et al. (2012a) investigated gullies in the Argyre Basin with a general age of <~20 Ma and an even younger generation of gullies with ages of about <500 ka.

Multi-temporal high-resolution image datasets of the last martian years (MY) offer the possibility to identify present-day seasonal modifications of gullies on Mars. For instance, bright sedimentary deposits at gully sites formed within the last decade imply current activity (Malin et al., 2006). These deposits show morphological attributes expected from liquid water flow (Malin et al., 2006; Heldmann et al., 2010), but they might also be consistent with dry flows (Pelletier et al., 2008; Kolb et al., 2010) or frosted granular flows, being lubricated by vaporization of CO_2 frost and possibly small amounts of H_2O frost (Hugenholtz, 2008).

A large variety of currently active mass movement features occur on dune slopes on Mars (e.g., Diniega et al., 2010; Reiss et al., 2010). These mass movement features do not share all morphological attributes and thus are morphological different to the classical gullies on Mars. Nevertheless, the same processes might trigger their present-day activity resulting in observable modifications of classical gullies.

Investigations of classical gullies (Dundas et al., 2010) show that present-day activity occurs in a latitude range between ~29°S and 54°S in 10 different regions on Mars, possibly involving CO_2 frost (Dundas et al., 2010). Interestingly, all these regions with present-day gully activity are located in latitude bands where H_2O and CO_2 frosts are seasonally stable (Vincendon et al., 2010a, 2010b). Activity of classical gullies in the last martian years in the southern polar regions and also in specific location presented in this work were detected by Dundas et al. (2012) and Raack et al. (2012b), however, it remains unclear how the activity was initiated. Dundas et al. (2012) and Raack et al. (2012b) narrowed the activity down to southern early spring and mid-spring, respectively. Generally, all seasonal activity of gullies occurred when defrosting, CO_2 ice sublimation or sublimation/melting of H_2O ice (brines) on the surface took place (Dundas et al., 2012).

Defrosting dark spots on large dark dunes were analyzed by several authors (e.g., Cantor et al., 2002; Piqueux et al., 2003; Kieffer et al., 2006; Appel et al., 2010). These dark spots are likely formed by basal sublimation of CO_2 ice followed by degassing of CO_2 gas through cracks within the translucent CO_2 ice slab, carrying darker sand and dust from the surface aloft to form dark spots on top of the slab ice (e.g., Piqueux et al., 2003; Kieffer et al., 2006).

Another model describes the formation of dark spots and the resulting dark flows on dunes in the northern polar region by basal melting of H_2O ice and subsequent seeping to the surface (Appel et al., 2010). Dark flows emanating from dark spots down the dune were also observed by, e.g., Kereszturi et al. (2009, 2010, 2011), Gardin et al. (2010), and Hansen et al. (2011, 2012). The formation of the dark flows is not yet understood. A proposed mechanism is the formation through the involvement of H_2O (Appel et al., 2010; Kereszturi et al., 2009, 2011) or brines (Kereszturi et al., 2010). Hansen et al. (2011, 2012) favored a formation through the involvement of CO_2, while Gardin et al. (2010) proposed avalanches of a mixture of sand, dust, and sublimating CO_2 ice above a frosted surface as the formation mechanism for the dark flows.

The most abundant volatiles on Mars are CO_2 and H_2O, which can be found in the atmosphere and in higher amounts as ices in the north and south perennial polar caps (e.g., Kieffer et al., 1976; Brown et al., 2010, 2012; Schmidt et al., 2010; Appéré et al., 2011) or in isolated and protected regions like impact craters (Brown et al., 2008). The seasonal changes in insolation result in a global volatile cycle characterized by waxing and waning of the seasonal polar caps due to seasonal deposition and sublimation of CO_2 and H_2O ices (e.g., James et al., 1992; Jakosky and Haberle, 1992). These seasonal processes might also lead to landform changes in the circumpolar regions on Mars (e.g., Christensen et al., 1998; Piqueux et al., 2003). The southern residual polar cap consists of a ~3700 m thick reservoir of H_2O ice and is covered the entire year by meters-thick CO_2 ice with contaminations of H_2O ice (e.g., Bibring et al., 2004a; Langevin et al., 2007). Completely CO_2-free H_2O ice was spectrally detected by Bibring et al. (2004a) during southern summer at the scarps around the residual polar cap and in regions tens of kilometers away from the CO_2 ice residual cap. Based on theoretical considerations, Farmer and Doms (1979) and Schorghofer and Aharonson (2005) suggested that a water ice layer can form down to ~30° latitude in both hemispheres. Recently, using near-infrared data, surface seasonal water ice has been detected on poleward slopes down to 13°S (Carrozzo et al., 2009; Vincendon et al., 2010a). Furthermore, evidence for near-surface perennial H_2O ice was obtained down to 25° latitude in the southern hemisphere (Vincendon et al., 2010b).

Here we report on seasonal modifications of a classical gully on a slope in the south polar pitted region named Sisyphi Cavi (71.5°S and 355°E). This region was selected because of the extensive coverage with high-resolution image data. With a multi-temporal survey of high-resolution images, temperature, and spectral data, we address the following main questions: (1) Which morphologic changes of the gully can be observed within the last martian years? (2) What is the time range (season) for the formation of new morphologic changes of the gully? (3) What material forms the morphologic changes? (4) What mechanism(s) triggers the formation of these new morphologic changes?

2. Study region

We have performed a survey of 130 HiRISE images acquired in the last four martian years (MY) in Sisyphi Cavi over a large area centered on 355°E and 71.5°S (Fig. 1). Fig. 1 shows a Mars Orbiter Laser Altimeter (MOLA) shaded relief model superposed by a MOLA digital terrain model. The black rectangles represent footprints of available HiRISE images; the red box represents the region with the gully showing morphologic changes (Fig. 2a). Almost half of the images cannot be used for our investigations because 41 images show no gullies and another 10 images are lacking multi-temporal coverage of at least two images. Most of the images used in this study were acquired during spring and summer.

The highest concentration of multi-temporal HiRISE images (36 images) is located at 1.3°E and 68.5°S (red square in Fig. 1, corresponding to Fig. 2a), thus, we will focus our study on this region. The study region comprises a polar pit with numerous gullies on

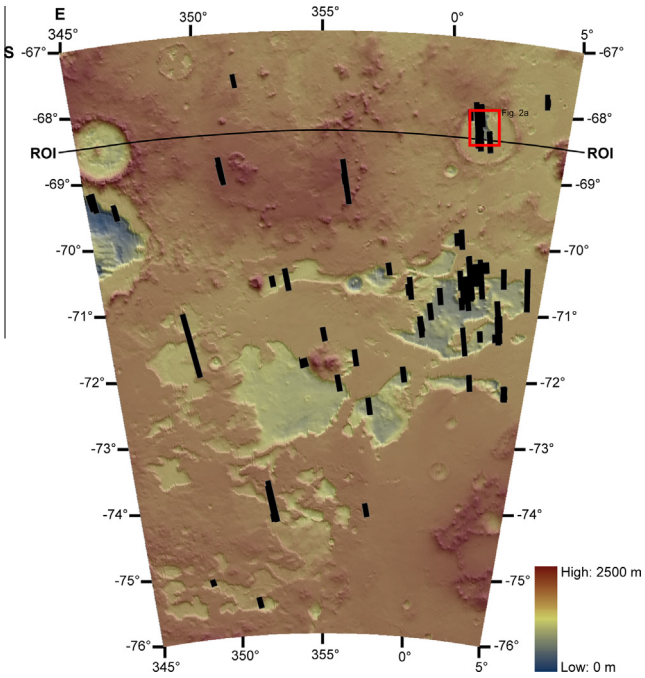

Fig. 1. Mars Orbiter Laser Altimeter (MOLA) shaded relief model superposed by a MOLA digital terrain model of Sisyphi Cavi. The color represents different topographic elevations from 0 to 2500 m (see legend). Black rectangles indicate footprints of all available 130 HiRISE images. The red box (see also Fig. 2a) indicates our study region. The continuous black line along 68.5°S latitude (region of interest-line) across Sisyphi Cavi is crossing the study region and represents the region of seasonal temperature and spectral measurements. (For interpretation of the references to color in this figure legend, the reader is referred to the web version of this article.)

its steep slopes within a large impact crater, which is partly filled with material (fine-grained material with enclosed boulders up to 5 m in diameter). The depth of the polar pit is up to ~1000 m. Ghatan and Head (2002a,b) proposed that polar pits in Sisyphi Cavi were formed by subglacial volcanoes east of Sisyphi Cavi and the basal drainage of meltwater. On the southern slope of the polar pit, seasonal morphologic changes of a single gully within the last three martian years were detected based on visual comparison of image datasets.

3. Data and methods

Martian seasons are defined by solar longitude (L_S), with L_S 180° representing the beginning of spring and L_S 270° the beginning of summer in the southern hemisphere. Martian years (MY) are numbered after the calendar proposed by Clancy et al. (2000) in which MY 1 began on April 11th, 1955. The High Resolution Experiment Primary Science Phase began at L_S 132° of MY 28.

3.1. HiRISE and CTX data, MOLA DTM

The investigations presented in this study are based on multiple data sets. Image data are provided by the High Resolution Imaging Science Experiment (HiRISE), and the Context Camera (CTX). Since November 2006, the Mars Reconnaissance Orbiter (MRO) has provided HiRISE images with a resolution of 0.25–1 m/pxl (McEwen et al., 2007) and CTX images with a resolution of ~5 m/pxl (Malin et al., 2007). Multi-temporal HiRISE images were used for identification of seasonal morphological changes of gullies and CTX images provided the geologic context of the study region. For detailed topographic information a HiRISE digital terrain model (HiRISE DTM) of images ESP_013097_1115 and ESP_013585_1115 with a resolution of 1 m/pxl was used (http://hirise.lpl.arizona.edu/dtm/dtm.php?ID=ESP_013097_1115). A Mars Orbiter Laser Altimeter digital terrain model (MOLA DTM) (Zuber et al., 1992) was used for context and topographic information of the entire study region.

All image datasets were processed with the Integrated Software for Images and Spectrometers (ISIS3), which is available from the U.S. Geological Survey (USGS). With ISIS3, the image files were radiometrically calibrated, normalized, stretched, map projected, and photometrically corrected.

Photometrically corrected CTX and HiRISE images were used to measure the surface albedo and to study its composition. For our analyses we corrected the images with the Lambert albedo model. This simple photometric model predicts that the surface scatters incident light uniformly in all directions. The HiRISE images were corrected for surface photometry using "photomet" during the processing of the image data with ISIS3.

Volume estimations were made with shadow measurements on HiRISE images. For the measurements we used the software "qview", an ISIS3 application to display .cub-files and perform interactive analyses, i.e., shadow measurements for estimations of heights, planimetry, and length measurements.

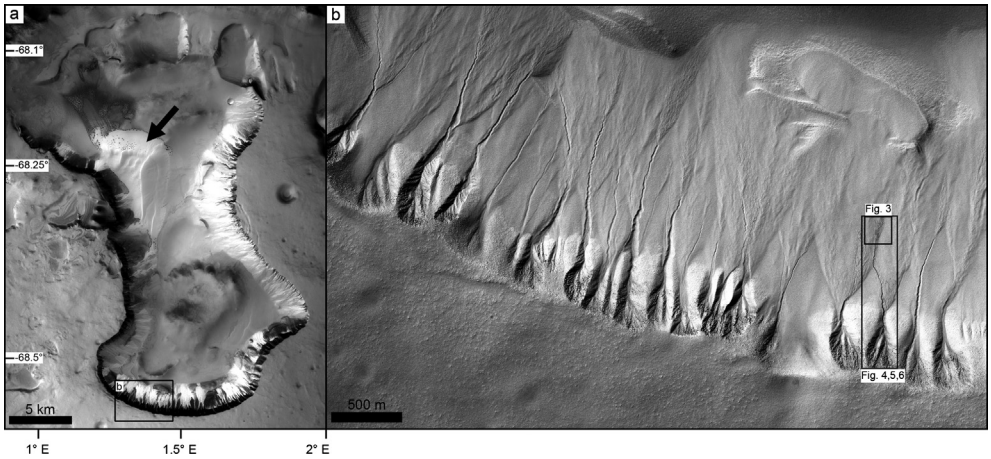

Fig. 2. (a) CTX image (B07_012332_1115) of the study region at L_S 227° in martian year 29. Gullies are located on all slopes of the polar pit. Within the polar pit a large dark dune is visible, which is covered by frost at these solar longitudes and therefore appears bright (black arrow). (b) Detail of the equator-facing slope in the southern part of the polar pit (HiRISE image ESP_013585_1115). The slope contains numerous gullies; the gully within the black box (see Figs. 3–6) represents the gully with dark flows and morphologic changes. North is to the top in all images.

3.2. TES and THEMIS data

Between 1998 and 2006 the Thermal Emission Spectrometer (TES) (~3 km/pxl) of the Mars Global Surveyor (MGS) mission provided thermal data (Christensen et al., 2001). These data were used for seasonal studies of daytime surface temperatures within the study region. The data were collected between ~1300 and ~1500 LMST (local mean solar time), the time range where maximum temperatures occur during a day. Therefore, "temperature" in the following sections and figures refers to maximum daytime surface TES temperatures.

TES temperature data were derived in earlier martian years than the identified morphologic changes (see also OMEGA data). However, this dataset provides the highest seasonal coverage of temperatures in the study region. Furthermore, large variations of surface temperature within the last couple of martian years are not expected (see Section 4.3 for details).

Temperature datasets were analyzed along the extended region of interest-line (ROI-line) close to our study region in longitude direction and at the same latitude to increase the seasonal coverage (see ROI-line in Fig. 1). We checked that surface temperatures measured at the exact study region (red square (Fig. 2a) in Fig. 1) were in good agreement with those measured along the extended ROI-line. Both measurements are comparable and show no large variations of temperatures.

TES temperature data were derived from the TES webpage of the Arizona State University (ASU) (http://tes.asu.edu/data_tool). TES data were processed online using the Vanilla software (http://software.mars.asu.edu/vanilla/index.html).

The Thermal Emission Imaging System (THEMIS) aboard 2001 Mars Odyssey (100 m/pxl) (Christensen et al., 2004) was used to determine relative local surface temperature variations on the illuminated slopes of the study region. All THEMIS Brightness Temperature Record (THEMIS-BTR) datasets were acquired by the THEMIS Processing Web Interface (http://thmproc.mars.asu.edu).

3.3. CRISM and OMEGA data

For spectral investigations we used near-infrared datasets provided by the Compact Reconnaissance Imaging Spectrometer for Mars (CRISM) (Murchie et al., 2007) and by the visible and infrared mineralogical mapping spectrometer (OMEGA) (Observatoire pour la Minéralogie, l'Eau, les Glaces et l'Activité) (Bibring et al., 2004b). CRISM aboard Mars Reconnaissance Orbiter provides near-infrared datasets with a resolution ranging between 18 and 200 m/pxl (Murchie et al., 2007). Since 2004, OMEGA aboard Mars Express acquired near-infrared spectral imagery with a resolution of 0.3–4.8 km/pxl (Bibring et al., 2004b). The spectral data of CRISM and OMEGA were used for identification of seasonal CO_2 and H_2O ices on the surface. To identify these surficial ices, the strength of the CO_2 ice absorption band at 1.43 μm and the H_2O ice absorption band at 1.5 μm were measured. These band strengths are complex non-linear functions of volatile amounts, grain size/texture, and mixture type (Langevin et al., 2007). Although OMEGA near-infrared data were acquired in earlier martian years than the identified morphologic gully modifications in image datasets and CRISM data, the OMEGA dataset was included in the investigations presented here to give a more detailed seasonal overview of the volatile behavior within the last couple of martian years. The spectral behavior is most likely comparable from one year to the next, as observed by Langevin et al. (2007) who measured similar H_2O and CO_2 spectra in different martian years. CRISM and OMEGA datasets were converted to Lambertian surface reflectance by dividing the radiance by the solar irradiance and the cosine of the incidence angle. To correct for absorption by atmospheric CO_2, we adopted the so-called volcano scan technique (New McGuire 2-wavelength (2007/1980)), as described in Bibring et al. (2005) and McGuire et al. (2009). The CO_2 and H_2O band strengths were measured by the diagnostic absorptions at 1.430 μm and at 1.510 μm, respectively, using the formulas described in Pelkey et al. (2007) for CRISM and in Langevin et al. (2007) for OMEGA. For the CRISM analysis only the "L" detector data (long wavelength, 1.0–3.9 μm; Brown et al., 2010) of the following datasets were used: MSP (multispectral mapping; ~200 m/pxl), HRS (half resolution short; ~36 m/pxl), HRL (half resolution long; ~36 m/pxl), and FRT (full resolution targeted; ~18 m/pxl) (Murchie et al., 2007). The OMEGA dataset consisted of the "C" channel (0.93–2.73 μm) observations with a swath width of 128 pixels, corresponding to a spatial resolution of above ~2 km/pxl (Forget et al., 2007). The CRISM data were analyzed using the CAT software for ENVI, and OMEGA data with the IDL software provided by the OMEGA team through the ESA Planetary Science Archive.

All datasets, image and spectral data, were imported into a Geographic Information System (ArcGIS), using a south polar stereographic map projection.

4. Results

4.1. Multi-temporal image analysis

We identified seasonal morphologic changes of a single gully in the study region (Fig. 2a) by comparing 26 HiRISE images of the last three MY. These changes occurred at the terminus of the gully channel at 1.44°E and 68.535°S on the southern slope of the polar pit within the study region (Fig. 2b). Within these three martian years, we detected two prominent seasonal morphologic changes.

4.1.1. Identified morphologic changes

Fig. 3 shows morphological changes at the terminus of the investigated gully channel in detail. At the beginning of spring (L_S 209°) in MY 29, we detected dark material within the gully channel. The terminus of the gully channel is marked with a black arrow #1 (Fig. 3a). Later, at mid-spring (L_S 226°), a well-developed dark flow-like feature extending ~70 m downhill on top of the apron is visible (Fig. 3b). At L_S 247° (mid/end of spring) a shortening of the channel of about several tens of meters due to infilling with material is detectable (Fig. 3c). The new gully channel terminus is marked with a black arrow #2. Furthermore, a small new deposit (small knob) is visible on the apron (white arrow). The strong early spring albedo contrast between dark flow and bright surroundings is no longer observed after L_S 247° (Fig. 3c, see also Figs. 4 and 5). One year later in MY 30 at L_S 218° (beginning of spring) dark material can be found within the channel, extending ~40 m downhill on top of the apron (Fig. 3d). At the end of spring (L_S 249°) of MY 30 there were no new deposits contrary to what was observed during the previous martian year. The small knob (white arrow) appears larger than in MY 29, but this could also be a photometric effect due to different solar illumination (Fig. 3e). Similarly, no new deposits or infilling are detected later in the season in MY 30 (Fig. 3f, end of spring/beginning of summer; L_S 277°). In MY 31 at L_S 215°, a dark flow-like feature on the apron is marked with a black arrow (Fig. 3g). The black horizontal lines represent the width of the gully apron. At L_S 226° a ~130 m long dark flow-like feature at the western side of the gully apron is detectable (Fig. 3h). This is comparable to the dark flow-like feature presented in Fig. 3b, which occurred at the same season two martian years earlier (MY 29). At mid-spring (L_S 236°), a new deposit at the western side of the gully is visible (black arrows; Fig. 3i). New material was deposited in the area where the dark

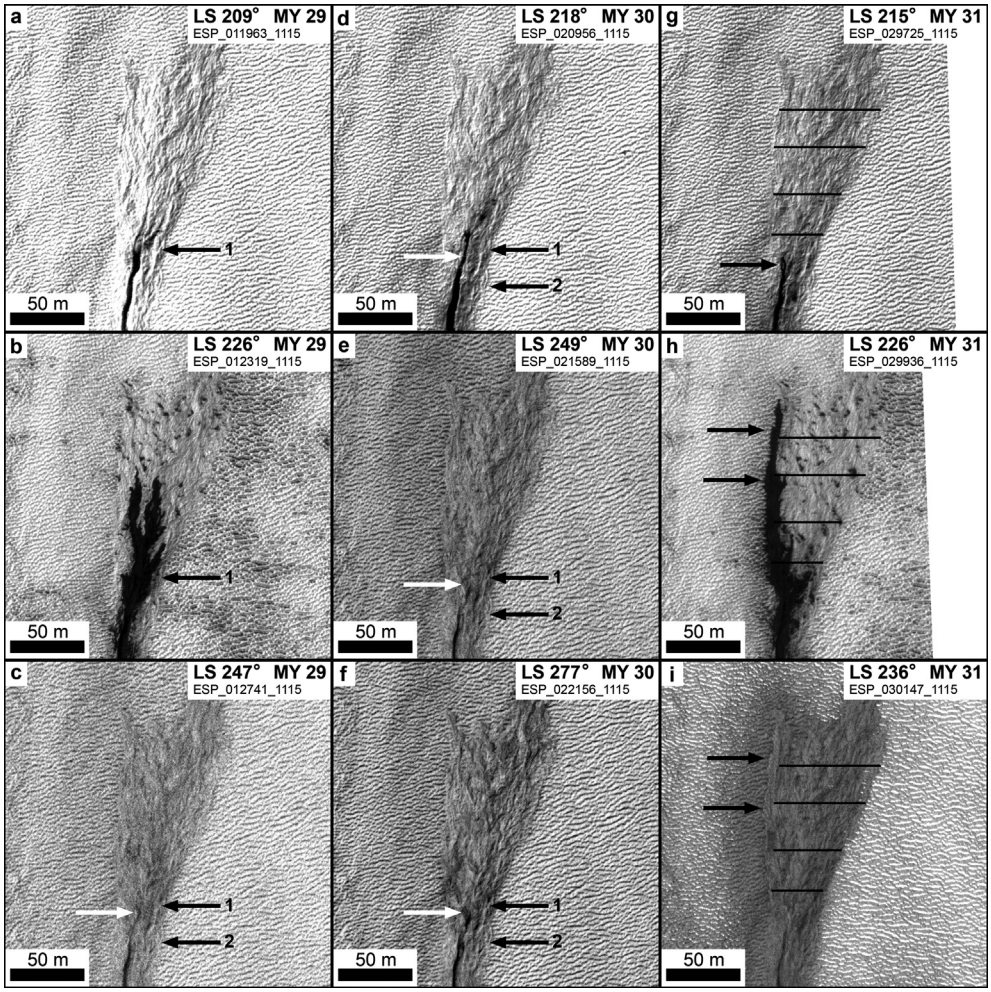

Fig. 3. Sequence of the seasonal changes in gully channel and apron morphology in martian years 29, 30, and 31. (a) Gully at L_S 209° in MY 29 (HiRISE image ESP_011963_1115). Arrow #1 marks the terminus of the gully channel. (b) Gully at L_S 226° in MY 29 (HiRISE image ESP_012319_1115). A dark flow superposes large parts of the apron. Arrow #1 marks the terminus of the gully channel at L_S 209°. (c) Gully at L_S 247° in MY 29 (HiRISE image ESP_012741_1115). Arrow #2 marks the new terminus of the gully. An infilling with material (white arrow) and a shortening of the channel is visible. (d) Gully at L_S 218° in MY 30 (HiRISE image ESP_020956_1115). Arrows are identical to those from MY 29. A small dark flow several tens of meters in length is superposed on the apron. (e) Gully at L_S 249° in MY 30 (HiRISE image ESP_021589_1115). Arrows are identical to those from MY 29. There is no new deposition of material. (f) Gully at L_S 277° in MY 30 (HiRISE image ESP_022156_1115). Arrows are identical to those from MY 29. We did not observe any further modifications. (g) Gully at L_S 215° in MY 31 (HiRISE image ESP_029725_1115). The end of a dark flow is marked with a black arrow. Four horizontal black lines represent the width of the gully apron. (h) Gully at L_S 226° in MY 31 (HiRISE image ESP_029936_1115). Horizontal black lines are identical to those from L_S 215°. The two black arrows mark the dark flow at the western flank of the gully apron. (i) Gully at L_S 236° in MY 31 (HiRISE image ESP_030147_1115). Horizontal black lines and black arrows are identical to those from L_S 215° and L_S 226°, respectively. Black arrows at L_S 236° mark new deposition at the western flank of the apron, which is deposited in the area the dark flow occurred at L_S 226°. North is to the top in all images.

flow-like feature occurred at L_S 226° (Fig. 3h). The black horizontal lines illustrate a widening of the apron of approximately 7 m.

4.1.2. Seasonal observations and albedo investigations

A detailed view of the investigated gully is shown in Figs. 4 and 5. The small alcove of the gully with morphologic changes is located in a depression. This depression is an older, larger gully alcove, which was most likely filled with material (dust–ice material). The younger, small gully alcove appears dark in Fig. 4a and b shows bright surroundings. The bright surroundings are located within the older, larger gully alcove.

Furthermore, Fig. 4 shows the seasonal morphologic changes of the entire gully during spring for the martian years 29 and 30. Fig. 4a, c, e, g and i shows stretched, grayscale HiRISE images of the gully and Fig. 4b, d, f, h and j the equivalent images as Lambert albedo values linearly stretched between 0 and 0.45. At the beginning of spring (L_S 209°) in MY 29 the interior of the gully alcove and the gully channel have a low albedo (Fig. 4a and b) (~0.25), while the surroundings have relative high albedo (~0.4–0.45). Regions with a high albedo correspond to surfaces covered with frost while regions with low albedo represent either relatively frost-free surfaces or icy surfaces contaminated with non-icy material. Alternatively, regions with low albedo can also represent small shadows or poorly illuminated local slopes not accounted for by the photometric correction. At L_S 227° in MY 29 (Fig. 4c and d), the dark flow within the gully channel shows a similar low albedo than the surroundings of the upper slope. The gully and its surroundings at L_S 227° (Fig. 4d) show lower albedos compared to L_S 209° (Fig. 4b). At mid/end of spring (L_S 247°), no dark regions are visible; the gully and the surroundings show identical low albedos of ~0.2, suggesting complete frost-free surfaces (Fig. 4e and f). One year later, at the beginning of spring in MY 30 (L_S 218°) surfaces with high albedo (~0.35–0.4) are visible in the alcove and in the northern part of the image (Fig. 4g and h). To summarize, Fig. 4a, b (L_S 209°), g, h (L_S 218°), and c, d (L_S 227°) shows a sequence of defrosting stages of the gully and its surroundings in MY 29 and 30. At

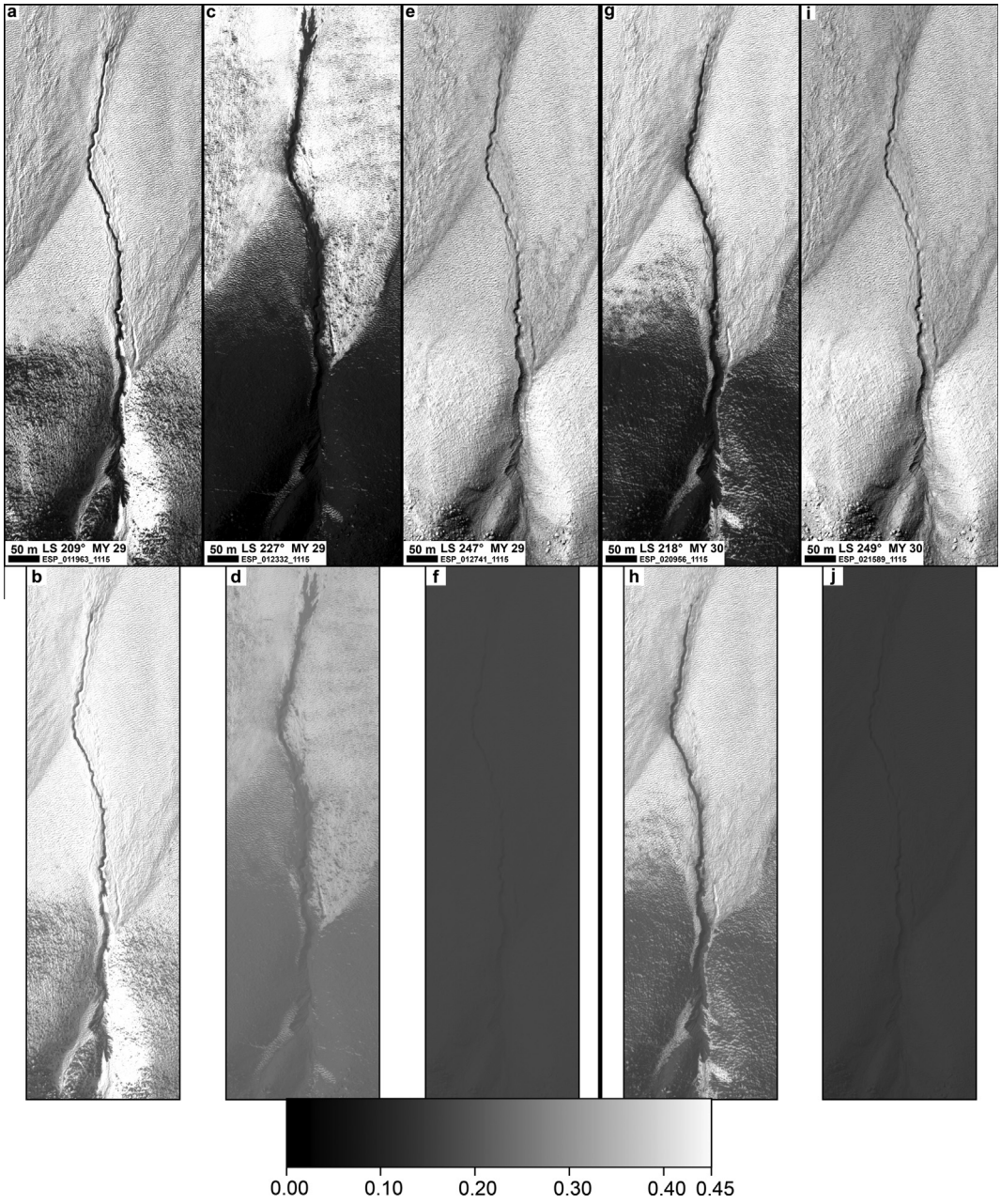

Fig. 4. HiRISE images (top) of the entire gully at different solar longitudes in MY 29 and 30 (a, c, e, g and i). The images below show Lambert albedo images of the same areas (b, d, f, h and j). The Lambert albedo images were linearly stretched between 0 and 0.45 (see legend at the bottom). They represent a sequence of different defrosting stages, starting at L_S 209° in MY 29 (a and b) and at L_S 218° in MY 30 (g and h) where frost on the surface covers large regions (bright areas). (c and d) Show the dark flow at L_S 227° in MY 29. At L_S 247° and L_S 249° in MY 29 and 30, respectively, all surfaces have a low albedo of ~0.2 (e, f, i and j). North is to the top in all images.

mid/end of spring (L_S 249°) in MY 30, no surfaces with high albedo are visible (Fig. 4i and j); the surface is completely defrosted and this is similar to the defrosting in MY 29 (Fig. 4e and f).

Fig. 5a–i shows a sequence of seasonal albedo changes of the gully during martian year 31. The stretching is equivalent to the Lambert albedo in Fig. 4, i.e., ranging between 0 and 0.45. From the end of winter to the beginning of spring (L_S 167°, 173°, 183°; Fig. 5a–c) an increase in Lambert albedo is detectable. At L_S 199° (Fig. 5d), new low albedo areas (~0.25) within the gully alcove and the gully channel are visible (black arrows). The equator-facing, steep upper slopes show low albedos comparable to the albedo within the gully channel (white arrow). At L_S 209° (Fig. 5e) the entire gully alcove and channel have a low albedo (~0.23–0.25) (black arrow). The white arrow in Fig. 5e points to bright regions with a high albedo (~0.34–0.4) next to the small gully apron (black arrow), implying a frost covered surface. At L_S 215° (Fig. 5f) the low albedo gully alcove with adjacent high albedo regions is visible. The younger, small gully alcove with a low albedo (black arrows in Fig. 5d and e) erodes the material within the older, larger gully alcove. Furthermore, in Fig. 5f some regions adjacent to the gully channel show a lower albedo (~0.34) (black arrow) than the surroundings (~0.4). At L_S 226° (Fig. 5g) and L_S 229° (Fig. 5h) these regions with a low albedo adjacent to the gully channel increase (black arrows). The entire upper slope region of the gully shows a low albedo except for some small areas with a higher albedo within the older, larger alcove (white arrows in Fig. 5g and h). These areas with a higher albedo represent remnants of the frost cover. At L_S 236° (Fig. 5i) the entire region shows the same low albedo (~0.18–0.19), implying a complete defrosting of the surface.

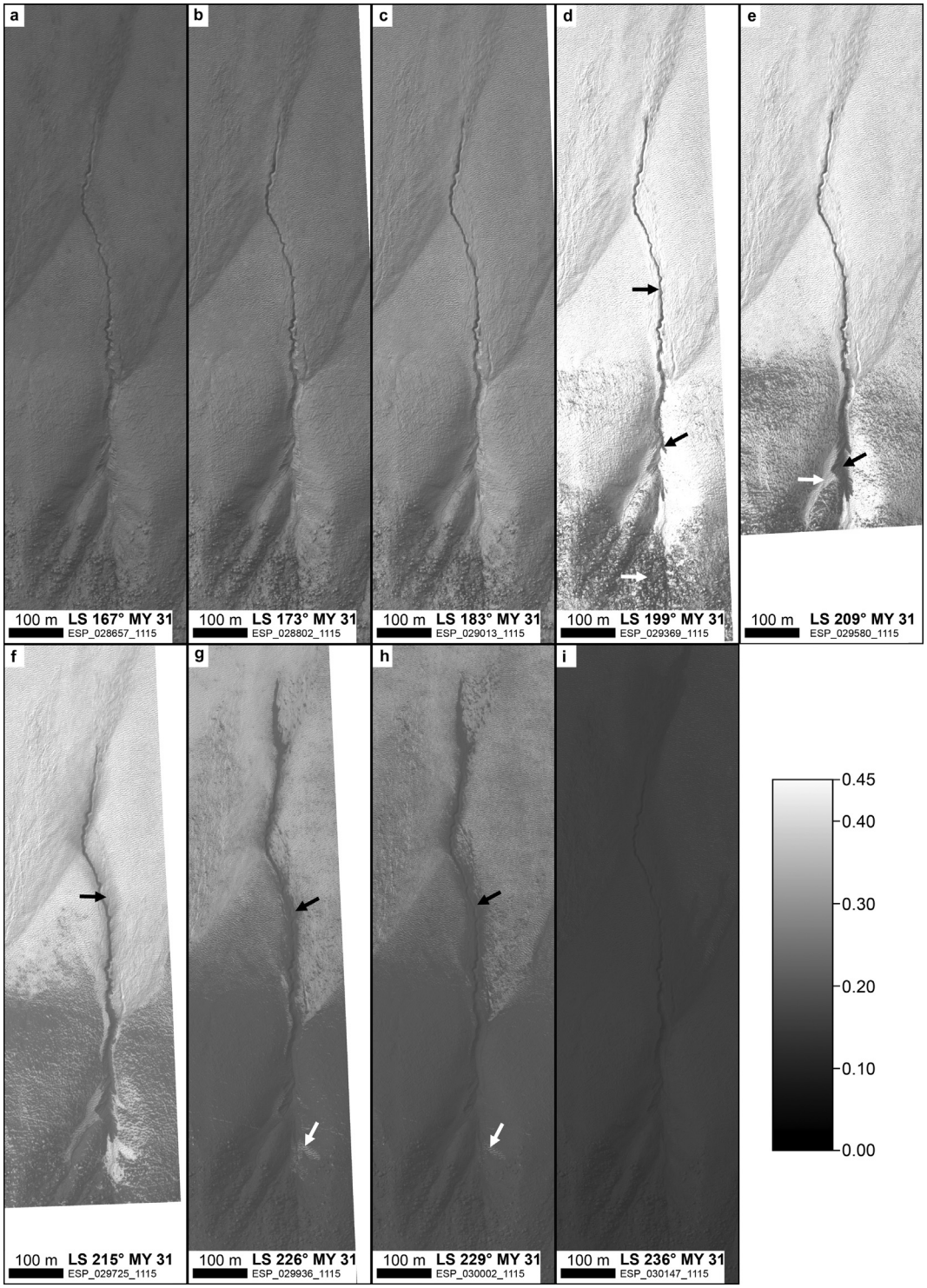

Fig. 5. Sequence of nine Lambert albedo HiRISE images of the entire gully in MY 31 (a–i). The images were stretched linearly between 0 and 0.45 (see legend on the right side) and are comparable with Lambert albedo images in Fig. 4. The first image (a) was acquired at the end of southern winter (L_S 167°), the last image (i) shows the albedo in mid-spring at L_S 236°. Black arrows in (d) show low albedo areas within the gully channel, the white arrow points to comparably low albedo areas on the steep upper slope. Black arrow in (e) shows low albedo areas within the gully alcove. The white arrow in (e) points to bright regions next to the small and dark gully apron. In (f) (L_S 215°) the black arrow shows regions with lower albedo next to the gully channel compared to their surroundings. These regions with lower albedo adjacent to the gully channel expanded at L_S 226° and L_S 229° (black arrows; g and h). The white arrows of (g and h) point to remnants of bright regions next to the gully alcove. At L_S 236° (i) the surface has a low albedo of ~0.18–0.19. North is to the top in all images.

4.1.3. Mapping

To identify the source of the dark material forming the dark flow, a sequence of maps of defrosting stages during early spring of MY 29 was used (Fig. 6). From L_S 183° to L_S 199° (Fig. 6a–c), areas with low albedo increase within the gully channel. Dark spots on the slope of the gully channel (Fig. 6a) change to small dark

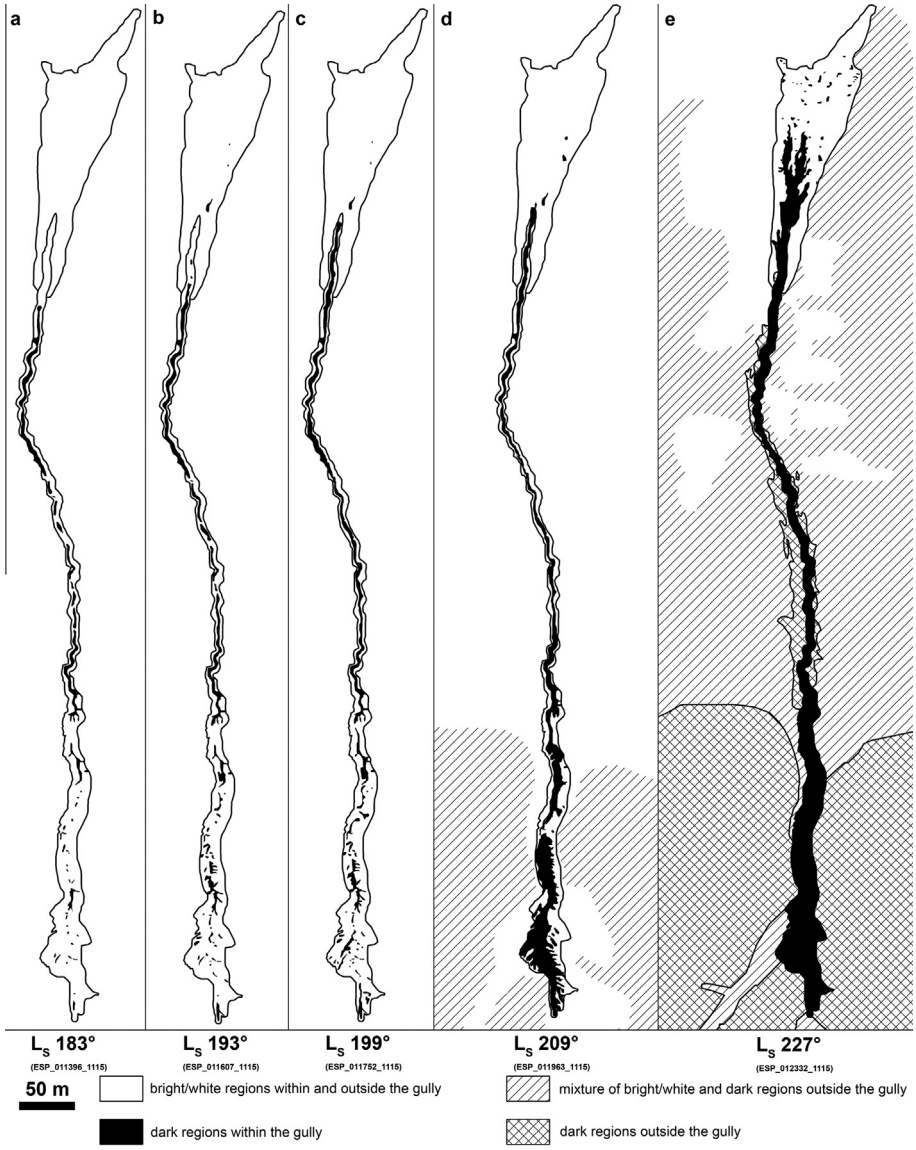

Fig. 6. Sequence of maps based on HiRISE images of MY 29 from L_S 183° to 227° (Fig. 6a–e). The maps show four different units. The shape of the gully with alcove, channel, and apron is outlined with a black line. The white unit shows regions with high albedo within and outside the gully, while the black unit represents low albedo areas within the gully (dark flows). Outside the gully, regions with a mixture of bright and dark regions (bright areas with small dark spots/regions) have a hatched pattern in the map. This unit is also presented in the Lambert albedo image Fig. 4b (light gray unit with an albedo between ~0.3 and 0.4 and visible low albedo spots). Areas with a crosshatched pattern in the map represent regions with low albedo outside the gully, also presented in the Lambert albedo image Fig. 4d (gray unit with a low albedo between ~0.1 and 0.2). North is to the top in all maps.

flow-like features with lengths of several meters (Fig. 6c). The dark regions within the gully channel expand in images between L_S 183° and L_S 209° (Fig. 6a–d).

Comparing images taken at L_S 199° and 209° (Fig. 6c and d), we find a very rapid darkening of the surface within the alcove and at the beginning of the channel. In addition, at L_S 209°, the surface with the steepest slopes surrounding the gully shows dark regions on top of wind ripple surfaces (hatched regions on the map of Fig. 6d). In Fig. 6e (L_S 227°), the complete gully apron and channel show low albedo surfaces as well as a dark flow feature on the apron (black areas). Furthermore, some regions adjacent to the gully channel, but outside the channel, have a low albedo surface such as the regions south of the gully (crosshatched pattern).

Investigating the gully alcove and channel with HiRISE images, we cannot directly verify erosion of material within small outcrops at the slopes of the gully channel and alcove. It is most likely that the erosion is shallow and, therefore, not observable with HiRISE imagery.

4.1.4. Volume estimations

To derive estimates of the volume of the deposited material, shadow measurements on HiRISE image ESP_013585_1115 (L_S 288°, MY 30) were performed. The newly deposited material is superposed on small ripples (Fig. 3i). In areas surrounding the gully alcove these ripples show heights of ~0.5 m. Making use of the HiRISE digital terrain model (Fig. 7), we measured the thickness of the gully apron superposing the rippled surface, which show heights of ~0.5–1 m. The newly deposited material on the western side of the gully alcove in MY 31 (Fig. 3i) covers an area of about 600 m^2. Assuming a thickness of the new deposit of about 0.5–1 m to cover the ripples, we find that ~300–600 m^3 of material were deposited in MY 31. However, due to limitations in

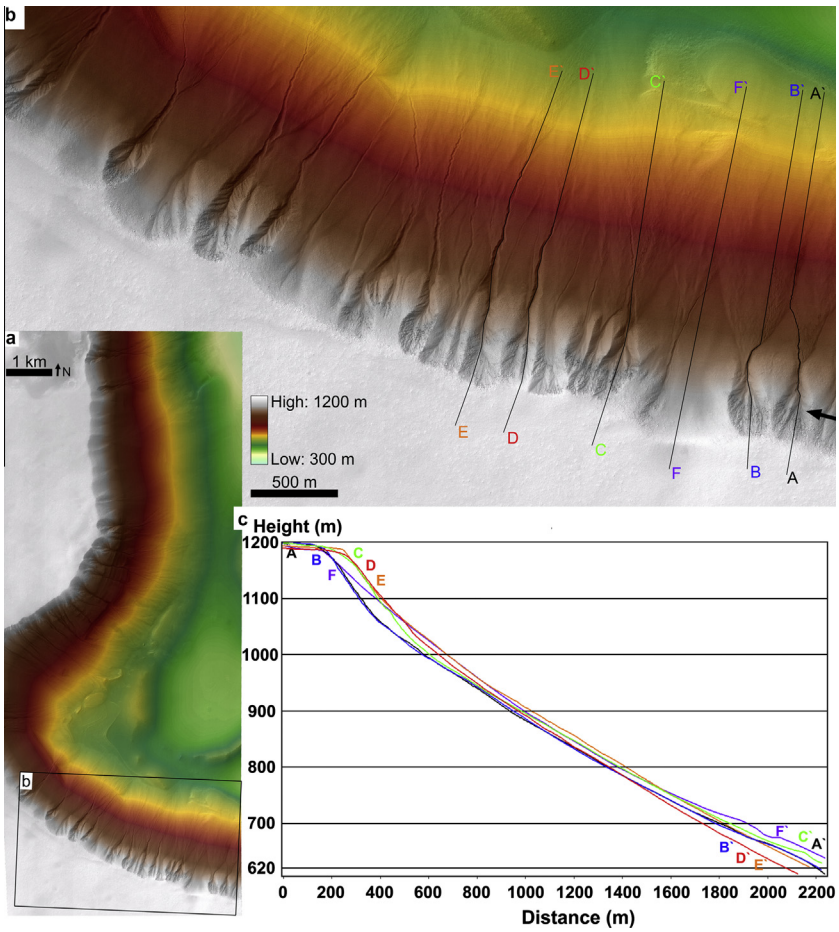

Fig. 7. HiRISE DTM (ESP_013097_1115) of the southwestern part of the polar pit (Fig. 7a). Colors represent topographic heights from 300 to 1200 m (see legend). (b) Shows the southern, equator-facing slope in detail. The observed gully with dark flows is marked at the eastern part of the image with a black arrow. Six different profiles were measured on the slope. (c) Shows the profiles (cross-section) of the slopes. Profile A–A′ (black) represents the profile of the gully with the dark flows, while profiles B–B′ to E–E′ represent profiles of adjacent gullies. The profiles were measured from top of the polar pit throughout the entire gully (alcove, channel, apron) to the bottom of the polar pit with a vertical exaggeration of about 2.3. Profile F–F′ (purple) represents the slope of the pit wall in between the gullies. Generally all profiles show a comparable mean slope angle of ~15°. North is to the top in all images. (For interpretation of the references to colour in this figure legend, the reader is referred to the web version of this article.)

determining the accurate thickness of the new deposit, this volume estimate needs to be treated with caution. Nevertheless, it serves as a first-order approximation of how much material was transported and deposited at the western flank of the apron.

4.2. Topography

To investigate the topography of the study region, we used a HiRISE digital terrain model (Fig. 7), derived from the HiRISE stereo pairs "ESP_013097_1115" and "ESP_013583_1115" (http://hirise.lpl.arizona.edu/dtm/dtm.phpID=ESP_013097_1115?). This digital terrain model was used to visualize the slope angles of the studied gully and adjacent gullies without modifications to find possible differences in topography and slope angle, which could have influence in the formation of the dark flows. The slope of the polar pit is very homogeneous and shows consistent topography and slope angles along its walls (Fig. 7a). Fig. 7b shows a detailed view of the slope with numerous gullies along the polar pit, including the investigated gully (black arrow). Profiles of five gullies were analyzed for their slopes (profiles A–A′ to E–E′; black, blue, green, red, and orange, vertical exaggeration of about 2.3; Fig. 7c). The profiles start at the flat plain above the polar pit and follow the gully to the bottom of the polar pit. Profile A–A′ (black) represents the gully with the dark flow. All profiles show comparable slopes and no obvious differences between the five gully slopes are visible. Profile F–F′ (purple) represents a profile of the slope in between gullies. Due to the lack of a gully alcove, this profile F–F′ shows small variations in form of a linear slope in the upper slope region compared to the concave upper slopes of the gullies (profiles A–A′ to E–E′). The average slope angle for all measured slopes is ~15°.

4.3. Temperature data

To identify possible mechanism(s) of the gully activity, maximum daytime surface TES temperatures of the study region and along the ROI-line were investigated. Fig. 8 shows maximum daytime surface TES temperatures from beginning of spring to early summer (L_S 180–300°). Red squares show surface temperatures within the study region (Fig. 1 (red box) and 2a) from 68°S to 68.7°S and from 0.7°E to 2°E. Black dots represent surface temperatures along the ROI-line between 345°E and 5°E (Fig. 1), the region of near-infrared spectral investigations. As seen in Fig. 8, both measurements are similar and show the same temperature trend, hence measurements along the ROI-line are approximately representative of surface temperatures within the studied polar pit.

It should be kept in mind that the TES temperatures represent surface temperatures of the study region, which were not directly derived at the gullied slope. Sun insolation on the steep slope can locally increase the surface temperature, but the measured TES

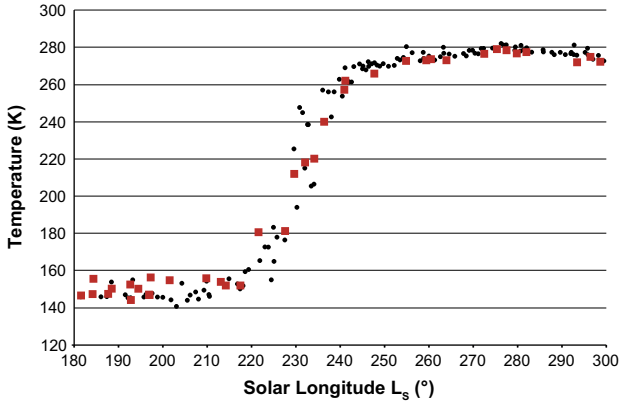

Fig. 8. Diagram with TES maximum surface temperatures from L_S 180° (beginning of spring) to L_S 300° (mid of summer). Red rectangles represent TES surface temperatures within the investigated polar pit; black dots show surface temperatures along the ROI-line (see Fig. 1). The comparable temperature trend of both regions shows that the ROI-line is representative of the smaller study region within the polar pit. (For interpretation of the references to colour in this figure legend, the reader is referred to the web version of this article.)

temperatures show mean surface temperatures of larger areas. THEMIS-BTR temperatures show relative variations of about +10 to +15 K on the equator faced gullied slope at the end of spring and in summer, indicating a higher surface temperature at the local gully sites as derived by TES.

TES surface temperatures at the beginning of spring are more or less constant at ~150 K, which is the condensation temperature of CO_2 frost at martian pressure conditions (Mellon et al., 2000; Steward and Nimmo, 2002). Between L_S ~210° and ~250°, a rapid increase of surface temperatures up to ~270 K occurs. This temperature rise is caused by increasing solar insolation and ice sublimation during spring in the southern polar region, leading to an increase of the area covered by defrosted terrains. As seen in Figs. 3–5 all flow-like features and modifications of gullies occur at times when daytime surface temperatures rise. From L_S ~250° to beginning of summer at L_S 280°, surface temperatures are relatively constant. The maximum surface temperature (~280 K) is reached at L_S ~280°. Surface temperatures decrease slowly with the beginning of summer (L_S ~290°).

At clear martian sky, the surface of Mars at ~68°S is shrouded in polar night up to L_S ~135° (Levine et al., 1977; Kuhn and Atreya, 1979), thus incident solar radiation is close to 0 cal/cm^2/day. The observed temperature increase at L_S ~210° occurs when the incident solar radiation reaches ~125 cal/cm^2/day (Levine et al., 1977; Kuhn and Atreya, 1979). Maximum surface temperature at L_S ~280° is reached when the incident solar radiation is also at its maximum between 250 and 300 cal/cm^2/day (Levine et al., 1977; Kuhn and Atreya, 1979).

4.4. Spectral investigations

4.4.1. Near-infrared spectral imagery

For a detailed analysis of CO_2 and H_2O band strength variations we investigated CRISM data of the investigated gully (Fig. 2b, Figs. 3–6). CRISM images FRT000053F5 (L_S 216° in MY 28) and FRT00011935 (L_S 227° in MY 29) are shown in Figs. 9 and 10, respectively. The band strengths in both images were stretched linearly between 0 and 0.45 for CO_2 and between 0 and 0.15 for H_2O. Fig. 9b and d, as well as Fig. 10b and d show detailed views of the gully area with the dark flow presented in Figs. 3–6. The white arrow shows the position of the dark flow that superposed the gully apron (Fig. 3). The southern equator-facing slope (including the investigated gully) of the polar pit shows relatively low CO_2 and H_2O band strengths, which were most likely caused by a higher solar insolation at these solar longitudes leading to an increased sublimation of these volatiles. The weaker band strength

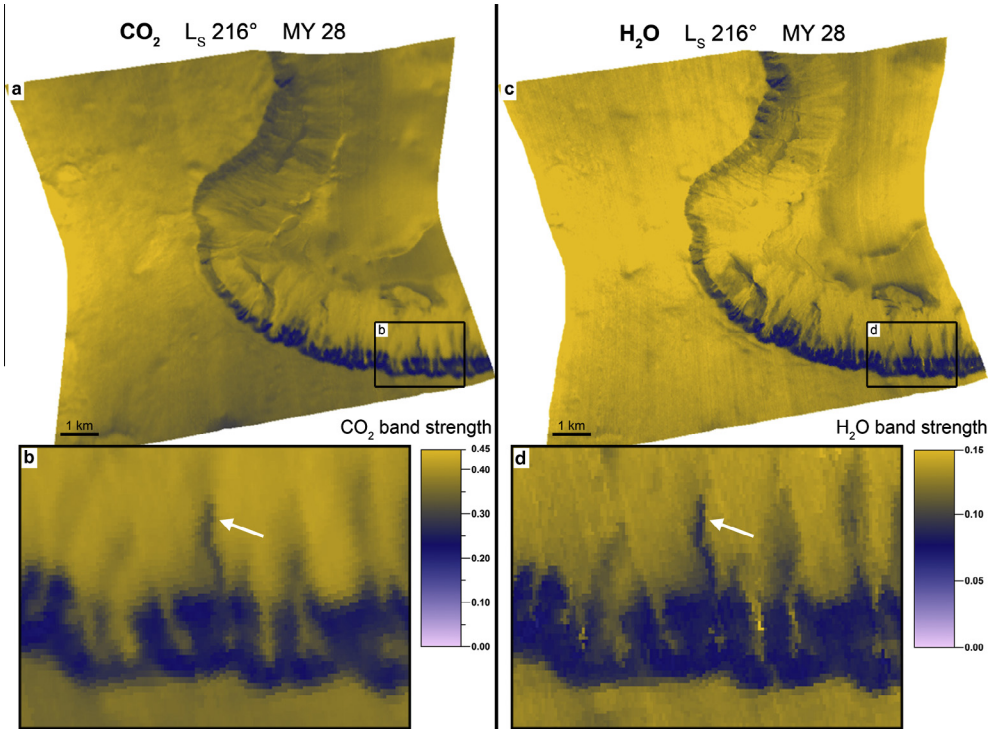

Fig. 9. Near-infrared spectral images of CRISM (FRT000053F5) of the southwestern part of the polar pit at L_S 216° in MY 28. (a and c) Show the area of the equator-facing slope; (b and d) are detailed views of the gully with the dark flow (white arrows). (a and b) Represent the band strength of CO_2 linearly stretched between 0 and 0.45; (c and d) show the band strength of H_2O linearly stretched between 0 and 0.15 (see legend). North is to the top in all images.

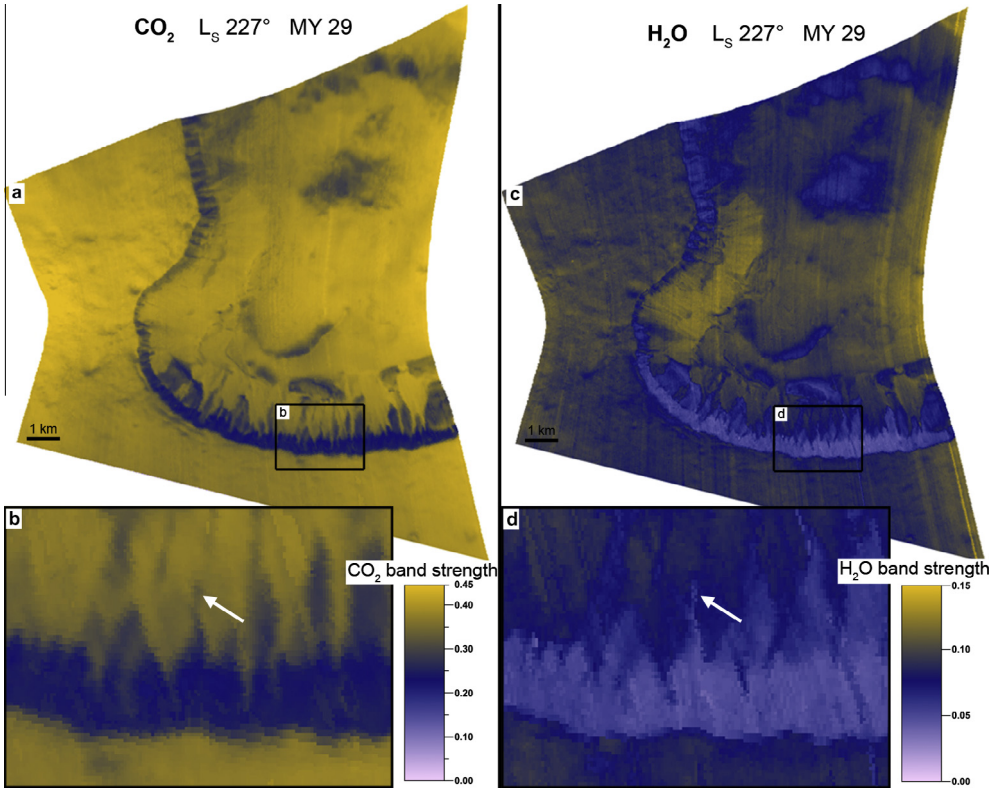

Fig. 10. Near-infrared spectral images of CRISM (FRT00011935) of the southwestern part of the polar pit at L_S 227° in MY 29 (comparable to HiRISE images/map in Figs. 3b, 4c, and 6e). The stretching is identical to Fig. 9 (between 0 and 0.45 for CO_2; and between 0 and 0.15 for H_2O). (a and b) Show band strengths of CO_2, while (c and d) show band strengths of H_2O. The white arrows points to the gully with the dark flow. Note that band strengths are generally lower compared to Fig. 9 because we are later in spring season. North is to the top in all images.

and therefore the presumably lower abundances of both volatiles on the surface within the investigated gully channel (Figs. 9 and 10; white arrows) are apparent. Adjacent gully channels show the same band strengths as their surroundings and are not visible in the near-infrared spectral CRISM images.

Regions with lower albedo correspond to regions with weaker band strengths of volatiles, indicating a larger proportion of non-icy material within or above the ice. However, while HiRISE albedo images might be interpreted to show that dark terrains are frost free, we can see in near-IR data that even dark terrains are characterized by relatively strong ice signatures during early to mid-spring.

A survey of the temporal evolution of CO_2 and H_2O was done by analyzing all available spectral datasets (CRISM: MY 28 and 29, OMEGA: MY 27, 28, and 29) at the ROI-line (68.5°S) between L_S 180° and 300° (Fig. 11) along with the associated smoothed maximum surface TES surface temperatures (black dotted line in Fig. 11). For CRISM investigations, we measured band strengths at 1.43 μm for CO_2 (red diamonds) and 1.5 μm for H_2O (blue diamonds) in an area of 1024 pixels on each CRISM image at latitudes of ~68.5°S. For each 1024 pixels region, the mean values of the band strength along with their minimum and maximum values were calculated. Mean values of band strength for both volatiles were also derived from OMEGA measurements for the same spectral parameters. We measured band strengths in 44 OMEGA images in a region from 65.4°S to 65.6°S along the ROI-line. The number of pixels for measurements varied between 24 pixels and 1012 pixels, depending on the coverage of the OMEGA image within the measurement area. In Fig. 11, OMEGA band depths of the 1.43 μm band (CO_2 ice) are shown as red squares, while blue squares represent band depths of the 1.5 μm band (H_2O ice). In order to compare spectral and surface temperature data with observed gully changes in MY 29–31, the time range of morphologic changes (Figs. 3–5) are shown as thick black lines above the graph in Fig. 11. CRISM as well as OMEGA data indicate decreasing band strengths of CO_2 and H_2O shortly after the large dark flows were observed, i.e., between both vertical dashed lines from L_S ~218° to ~226° in Fig. 11. It is important to understand that with both datasets one can only detect the last sublimation phases of volatiles on the surface. As long as the instruments do not measure the underlying surface and the superposed icy surfaces appear as an optically thick layer, sublimation of volatiles cannot directly be detected. Band strengths decrease when locally defrosted areas appear within a pixel. This rapid decrease of band strengths is visible between L_S ~220° and ~245° in Fig. 11. It is possible that the sublimation of both volatiles started much earlier than the decrease of band strengths is visible, likely between both vertical dashed lines from L_S ~218° to ~226° (Fig. 11) when dark flows occur.

4.4.2. Spectral modeling

Spectral modeling is used to estimate the percentage of terrains covered with optically thick regolith within CRISM pixels assuming a spatial subpixel mixing between regolith-covered and ice-covered terrains (see Fig. 12). This assumption relies on the fact that ice-covered terrains as well as defrosting terrains imaged by HiRISE images show a patchy appearance with patches of dark regolith-covered terrains surrounding bright ice-covered terrains at a scale lower than the resolution of CRISM instrument (~18 m/pxl). If this surface representation is correct, i.e., a subpixel mixing between regolith-covered and ice-covered terrains, then each CRISM spectrum of a given CRISM cube can be fitted by a linear

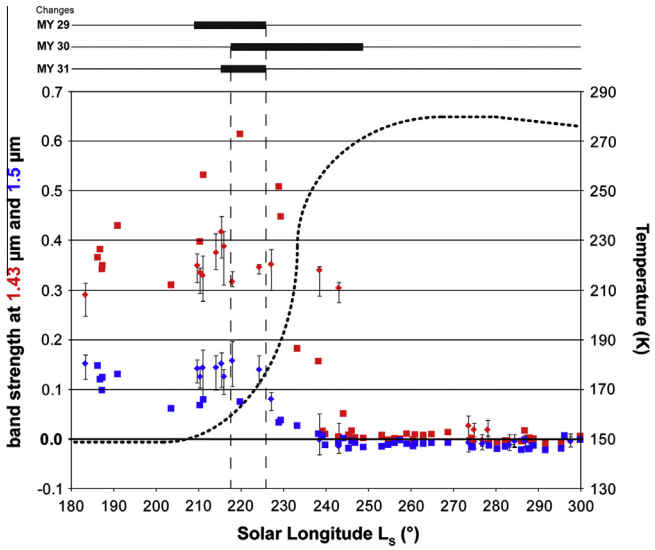

Fig. 11. Diagram of band strengths at 1.43 and 1.5 µm and temperatures versus solar longitude (L_S). The three thick black lines on top of the graph represent the identified morphologic and albedo changes of the gully during MY 29–31, i.e., the time range when the dark flows formed (Fig. 3). The time period of the appearance of the dark flow can be narrowed down between L_S 218° and L_S 226° in these three martian years (vertical dashed lines). The black dotted line represents the maximum daytime surface temperatures of TES along the ROI-line, which is also presented in Fig. 9. Near-infrared spectral measurements of absorption band strengths at 1.43 µm (CO_2 ice) and at 1.5 µm (H_2O ice) along the ROI-line are represented in red and blue, respectively. Diamonds indicate CRISM measurements, while squares represent OMEGA measurements. CRISM measurement vertical bars correspond to the minimum and maximum variations within the area of measurements (1024 pixels). Negative values of CRISM and OMEGA data are due to observation and instrumental noise. We observe that the dark flows occur when surface temperature begins to rise very rapidly and volatiles (CO_2 and H_2O ice) sublimate. (For interpretation of the references to colour in this figure legend, the reader is referred to the web version of this article.)

combination between (i) the spectrum of the regolith-covered terrain and (ii) the spectrum of CO_2 ice-covered terrain. As shown in Fig. 12, two different scenarios can result in subpixel mixing between the regolith spectral signature and the CO_2 ice spectral signature: (i) spatial mixing between completely defrosted terrains and ice-covered terrains at a scale lower than the pixel size (Fig. 12a), or (ii) spatial mixing between an ice layer covered by an optically thick regolith cover (Fig. 12b). It is important to note that our spectral modeling cannot make the distinction between these two options.

The regolith endmember spectrum was taken from the CRISM cube FRT00007D1E acquired in southern summer (L_S 318°) next to the polar pit region in MY 28. This spectrum shows an albedo of ~0.3 in the continuum between 1 µm and 2.5 µm. The CO_2 ice endmember spectrum was taken from the CRISM cube FRT000053F5 acquired in southern spring (L_S 216°, MY 28) within the study region. The spectrum chosen for the CO_2 ice endmember shows strong CO_2 ice absorption bands and a high albedo of ~0.55 in the continuum between 1 µm and 2.5 µm, indicative for a translucent CO_2 ice cover with minor contaminations of dust.

A library of spectra s^{lib} was built by computing the linear combination between the "regolith" and the "CO_2 ice" endmembers. We considered 101 combinations ranging from 0% to 100% of the surface covered by the CO_2 ice spectral signature with a step of 1%. For each CRISM spectrum s^{obs}, we looked for the closest neighbor in the library by defining a chi-square value χ^2:

$$\chi^2(s^{obs}, s^{lib}) = \frac{\Sigma_\lambda \omega_\lambda (s^{obs}_\lambda - s^{lib}_\lambda)^2}{\Sigma_\lambda \omega_\lambda}$$

s^{obs}_λ and s^{lib}_λ correspond to the reflectance factor at the wavelength λ for the observed CRISM and the library spectrum, respectively. χ^2 are computed for wavelengths ranging between 1 and 2.5 µm. The weights w_λ allowed us to put more emphasis on key spectral features such as CO_2 ice absorption bands or were set equal to zero to exclude dead and hot spectels and those for which the atmospheric correction is not optimal. The best fit of the library spectrum to the CRISM spectrum corresponds to a minimum χ^2 value.

The percentage of regolith-covered terrain within each CRISM pixel was estimated for the two CRISM images covering the study region in spring: FRT000053F5 (L_S 216°, MY 28, Fig. 9) and FRT00011935 (L_S 227°, MY 29, Fig. 10). Fig. 13 shows the results of this inversion. Fig. 13a and c shows the percentage of regolith-covered terrain within each CRISM pixel for CRISM image FRT000053F5 and FRT00011935, respectively. A detailed view of the gully with the dark flow is also provided in each image of Fig. 13. In particular, Fig. 13b and d show the χ^2 value corresponding to the best fit, i.e., the linear combination of regolith spectral signature and CO_2 ice spectral signature that best fits an individual CRISM spectrum. A χ^2 value lower than 500 corresponds to a good fit, while a χ^2 greater than 600 is indicative of a bad fit. Relatively low χ^2 values (lower than ~400) are obtained on the equator-facing slope except for poorly illuminated areas. In particular, good fits are obtained on the gully with the dark flow and its surroundings for both CRISM images. Medium χ^2 values are obtained on the plateau above the gullies. The higher χ^2 values and thus the worst fits are obtained for the pit floor and for the eastern part of the image (Fig. 13b and d).

Comparison between Fig. 13a and c shows that the spatial extension of regolith-covered terrains is higher in Fig. 13c than in Fig. 13a. The sublimation of Mars' south polar seasonal cap has been shown to slightly vary between years (Titus and Kieffer, 2002; Langevin et al., 2010). The date of "Complete Recession of CO_2 Under Sublimation" (CROCUS) at a given location can typically change by a few degrees of solar longitude between years. Unfortunately, good CRISM seasonal coverage of our region has only been obtained over several years, which means that differences between images include both annual and seasonal differences. Fig. 13a and c correspond to L_S 216° (MY 28) and L_S 227° (MY 29); as the time gap between these two images (11° of L_S) is larger than typical inter-annual variability timescales (a few degrees of

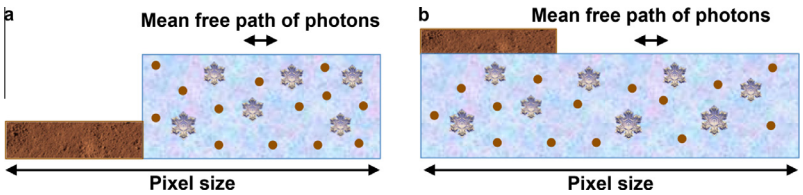

Fig. 12. Schematic sketch of two scenarios resulting in spatial subpixel mixing between the spectral signatures of regolith and CO_2 ice. (a) Spatial mixing between completely defrosted terrains and icy terrains at a scale lower than the pixel size. (b) A CO_2 ice layer partly covered by an optically thick regolith cover at a scale lower than the pixel size. The mean free path of photons is smaller than the thickness of this top regolith layer. Small flakes and brown circles respectively represent water ice particles and dust particles included in the CO_2 ice slab.

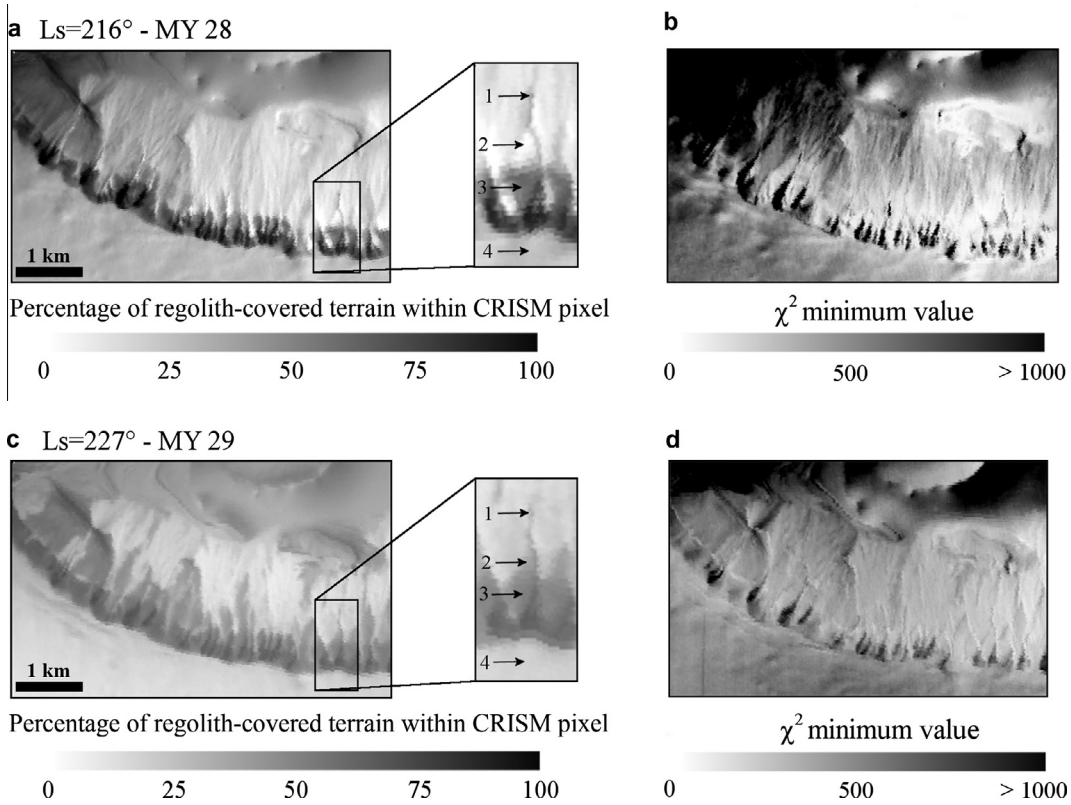

Fig. 13. Estimation of the percentage of regolith-covered terrain within each pixel for CRISM cubes FRT000053F5 (a) and FRT00011935 (b). Detailed views of the gully with the dark flow are shown as inserts. The four black arrows indicate the location where spectra of Fig. 14 were extracted: (1) terminus of the gully channel, (2) terrain adjacent to the gully channel, (3) terrain adjacent to the alcove and (4) plateau above the gully. (b and d) Show the minimum value of χ^2 obtained during the inversion of the regolith coverage for CRISM cubes FRT000053F5 and FRT00011935, respectively. For each pixel, this χ^2 minimum value corresponds to the best fit, i.e., the linear combination of regolith spectral signature and CO_2 ice spectral signature that best fits an individual CRISM spectrum.

L_S; Titus and Kieffer, 2002), we will consider that the differences between these two images are mainly due to differences in L_S. Furthermore, we have demonstrated in Sections 4.1 and 4.3 that HiRISE and TES observations do not show significant inter-annual variability concerning the seasonal evolution of the materials.

The spatial extension of regolith-covered terrains, thus, increases between L_S 216° and L_S 227°. In particular, several bright spots on the upper equator-facing slope show 0–5% of regolith-covered terrains within CRISM pixels at L_S 216° (Fig. 13a, arrow at location 2), while the entire upper slope contains at least ~35% of regolith-covered terrains within CRISM pixels at L_S 227° (Fig. 13c, arrow at location 2). This is in agreement with the defrosting stages observed by HiRISE during MY 29, 30, and 31 (Figs. 3–5).

In order to quantify the temporal evolution of the gully with the dark flow, we extracted CRISM spectra and the corresponding best fits at four different locations (Fig. 14). Going upslope, these locations are: (1) terminus of the gully channel, (2) terrain adjacent to the gully channel, (3) terrain adjacent to the alcove and (4) plateau above the gully. The exact position of these locations is indicated in Fig. 13.

Fig. 14 illustrates that the CRISM spectra can be well reproduced by our spatial subpixel mixing between regolith-covered and ice-covered terrains. For each location, we observe only minor differences between spectra obtained at L_S 216° (MY 28) and at L_S 227° (MY 29) with the exception of location 2 where the continuum level drastically decreases between the two CRISM images. The level of the continuum slightly increases between the two CRISM images for locations 1, 3 and 4. This implies a minor decrease of the regolith coverage, of 5–8%, between L_S 216° and 227° at locations 1, 3 and 4. The exception is location 2 where the regolith coverage strongly increases.

The percentage of regolith-covered terrain within CRISM pixels associated with each location and L_S is indicated in Table 1. Our spectral mixing model indicates that the regolith coverage of location 2 increases from 3% to 36% of the surface between L_S 216° (MY 28) and L_S 227° (MY 29). We interpret this increase in regolith coverage next to the gully channel to either correspond to an increase of the surface covered by defrosted terrains, or to an increase of the regolith cover over the CO_2 ice layer (see Fig. 12).

Surprisingly, the regolith coverage decreases in location 1, at the terminus of the gully channel, between L_S 216° (MY 28) and L_S 227° (MY 29), whereas a lengthening of the dark flow is observed by HiRISE at L_S 227° in MY 29 (Figs. 3b and 4c). We also notice that the percentage of regolith-covered terrain decreases in location 4, i.e., on the plateau above the gully. Such behavior is not expected at this stage of the spring season and is very likely due to scattering by mineral aerosols. Indeed, Vincendon et al. (2007) showed that scattering by atmospheric dust lowers the albedo of bright icy surfaces and reduces its spectral contrast. Therefore, a variation in the dust content of the atmosphere between the two CRISM images may be responsible for the variation in the spectral signature of location 4. We thus assumed that the spectral signature of location 4 should be almost identical between L_S 216° (MY 28) and L_S 227° (MY29) after the effect of aerosol scattering is corrected. Then, for both CRISM images and for each location i (i = 1, 2, 3, 4), we computed the ratio between the percentage of regolith-covered terrain at location i and the percentage of regolith-covered terrain at location 4 (Table 1). With this method it is possible to compare the variation of the regolith coverage between

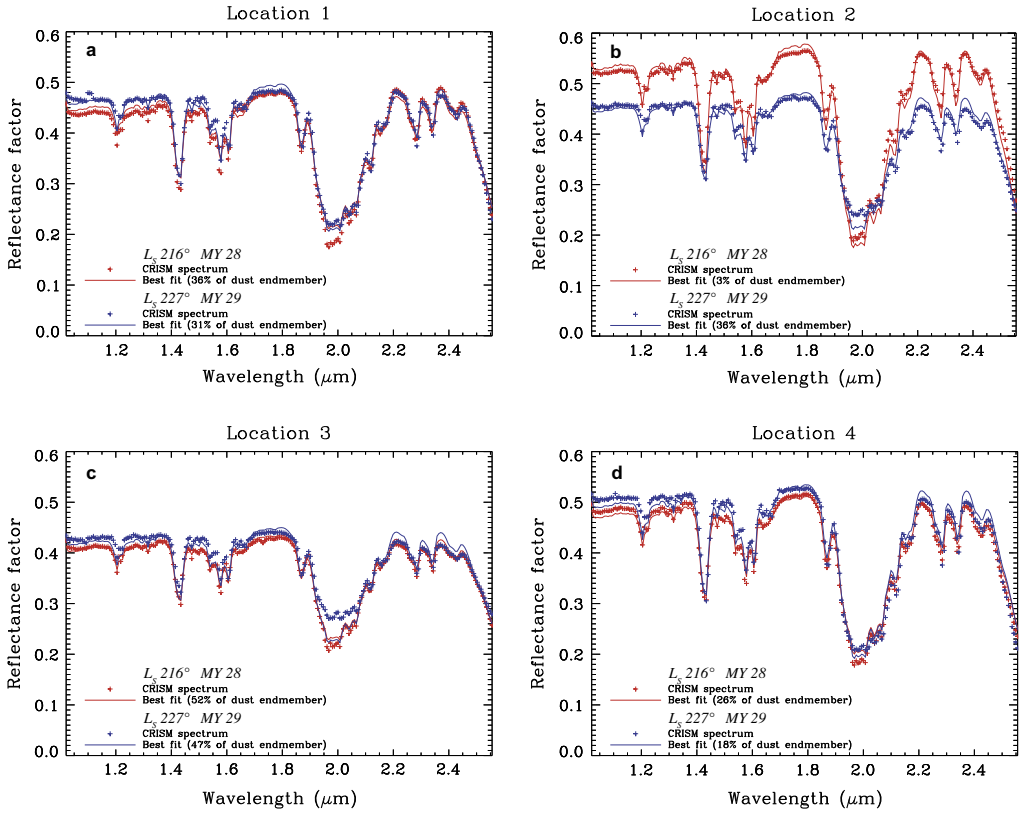

Fig. 14. CRISM spectra and their best fit extracted at the four locations indicated in Fig. 13. (a) Red crosses: CRISM spectrum extracted at location 1 (terminus of the gully channel) at L_S 216° in MY 28. Red line: best fit of CRISM spectrum extracted at location 1 at L_S 216° in MY 28. Blue crosses: CRISM spectrum extracted at location 1 at L_S 227° in MY 29. Blue line: best fit of CRISM spectrum extracted at location 1 at L_S 227° in MY 29. (b) Same as (a) but for location 2 (terrain adjacent to the gully channel). (c) Same as (a) but for location 3 (terrain adjacent to the alcove). (d) Same as (a) but for location 4 (plateau above the gully). (For interpretation of the references to colour in this figure legend, the reader is referred to the web version of this article.)

Table 1
Columns 2 and 3 show the percentage of regolith-covered terrain within each pixel for locations 1–4 for CRISM cubes FRT000053F5 (L_S 216°, MY 28) and FRT00011935 (L_S 227°, MY 29), respectively. Columns 4 and 5 show the ratio between the percentage of regolith-covered terrain at location i (i = 1, 2, 3, 4) and the percentage of regolith-covered terrain at location 4 for CRISM cubes FRT000053F5 (L_S 216°, MY 28) and FRT00011935 (L_S 227°, MY 29), respectively.

Location	Percentage of regolith-covered terrain at L_S 216° (%)	Percentage of regolith-covered terrain at L_S 227° (%)	Ratio between regolith coverage at location i and regolith coverage at location 4 for L_S 216°	Ratio between regolith coverage at location i and regolith coverage at location 4 for L_S 227°
1	36	31	1.38	1.72
2	3	36	0.12	2.00
3	52	47	2.00	2.61
4	26	18	1.00	1.00

L_S 216° (MY28) and L_S 227° (MY 29) relative to location 4. We find that in locations 1, 2 and 3, the regolith coverage with respect to location 4 increases between L_S 216° (MY 28) and L_S 227° (MY 29). In particular, at the terminus of the dark flow (location 1), the regolith coverage increases from 1.38 to 1.72 relative to location 4; next to the gully channel (location 2), the regolith coverage increases from 0.12 to 2.00 relative to location 4. On the terrain adjacent to the alcove (location 3), the regolith coverage increases from 2.00 to 2.61 with respect to location 4. This behavior is consistent with HiRISE observations documenting the evolution of the dark flow and its surroundings.

In summary, spectral modeling makes it possible to derive first order estimates of the percentage of regolith-covered terrain within each CRISM pixels. This regolith-covered terrain is either in the form of defrosted mineral terrain or consists of a regolith layer covering the CO_2 ice layer. Because of the lack of correction for aerosol effects, these values are minimum values for CRISM image FRT00011935 acquired at L_S 227° in MY 29.

5. Discussion

Analyses of multi-temporal images show present-day activity of a martian gully at 1.44°E and 68.54°S. Morphologic changes at the terminus of the gully channel in MY 29 and at the western side of the apron in MY 31 indicate transport and new deposition of material within these years. Defrosting histories and behaviors of the dark flows are comparable in all observed years. At the end of winter (L_S 180°), surface temperatures are constant at ~150 K. First morphologic changes are visible between L_S 183° and L_S 193°. Small patches of dark material occur on the slopes of the gully channel and of the apron, and accumulated within the channel. This dark material expands over time and continues to accumulate within the gully channel until L_S ~218°. At this time, surface temperatures increased to ~160 K. Between L_S 218° and 226°, dark flows are located in the entire gully channel and partially cover the apron. Lambert albedo observations, as well as near-infrared data show that the dark flows have weaker band strengths of

volatiles (CO_2, H_2O) compared to their surroundings. This is probably caused by the higher regolith content of the dark flows compared to their surroundings as shown by spectral modeling. Seasonal observations along the ROI-line at 68.5°S show an increase of surface temperatures within L_S 218° and 226° from ~160 K to ~180 K. At this time, the CO_2 ice and H_2O ice band strengths appear to be relatively constant. However, at this time CO_2 sublimation might have already begun, but cannot be detected with spectral data. At L_S 236°, first new deposits on the apron and within the gully channel are detectable. Volume estimates indicate that in MY 31 ~300–600 m^3 of material were deposited. Surface temperatures at L_S 236° reached ~245 K, showing a very rapid increase of about ~65 K between L_S ~226° and 236°. In addition, spectral analyses show a rapid decrease of volatile spectral signatures during this time period due to ongoing sublimation related to increasing solar insolation. Schmidt et al. (2010) also identified a rapid sublimation/defrosting of the surface after L_S ~220° of the anti-cryptic region, which comprises our study region. Around L_S 240–245° all CO_2 and H_2O frosts were completely sublimated in our study region. Surface temperatures reached ~260 K at these solar longitudes. No further deposition of material can be identified and albedo images show a completely defrosted surface. Surface temperatures of ~273 K were reached at L_S ~250°; maximum surface temperatures of ~280 K were reached at L_S ~280° (Figs. 8 and 11).

It is important to note that the present-day activity of the gully show ongoing modifications (dark flows and new deposits) of the gully. The overall formation process of gullies within polar pits in Sisyphi Cavi should not necessarily be linked to the following scenarios of present-day activity of our investigated gully. There are three scenarios that could explain the present-day modifications by dark flows within the gully: liquid water supported flows, CO_2 gas supported (lubricated) flows, and dry flows.

5.1. Liquid water supported flows

Conway et al. (2011) demonstrated in experimental investigations on Earth that fluid overland flows with erosion and transportation of material on Mars possibly only need smaller amounts of liquid water compared to Earth. This is related to freezing of water at cold martian conditions in the shallow substrate, impeding further infiltration (Conway et al., 2011). On this frosted and saturated subsurface, water cannot further infiltrate but will flow downstream on top of the frosted subsurface (Conway et al., 2011). Kereszturi et al. (2009, 2010, 2011) proposed a formation of dark flow-like features on dunes by interfacial water with a probable involvement of brines (Kereszturi et al., 2009). This dark flow activity was also observed when the surface is defrosting. Spectral CRISM observations by Kereszturi et al. (2011) showed that the dark spots on dunes contain H_2O ice on the surface. Reiss et al. (2010) also observed recent small linear gullies carved in the Russell crater dune field (54°S) and (based on channel morphology, spectral data and modeled surface temperatures) proposed slurry flows consisting of sand mixed with liquid H_2O as a formation mechanism. However, the activity of linear gullies on the Russell crater dune field is characterized by erosion of dune material. In our study we observed only depositional processes, i.e., we could not identify the exact source of the dark flows. In addition, surface temperatures are relatively high (up to ~270 K) when activity of the observed Russell crater gullies occurred, and are different from those temperatures observed for gully activity in our study region. In summary, in our study area formation of the dark flows related to liquid water is implausible because temperatures between ~160 and ~180 K (when the dark flow is detectable) are too low. Also even when we consider relative temperature variations of about +10 to +15 K (measured with THEMIS-BTR) due to different Sun insolation on the illuminated equator faced gullied slope, temperatures are not high enough to melt or sublimate H_2O ice. In our study region the melting point of ~273 K was reached at L_S ~250°, only after the formation of the dark flows. Although briny liquid flows have higher melting points, they require temperatures above ~200 K (Möhlmann, 2011), which are not yet reached at times when activity occurred in the study region.

5.2. CO_2 gas supported (lubricated) flows

CO_2 gas supported (lubricated) flows (e.g., Musselwhite et al., 2001; Hoffman, 2002) could be a scenario for the indentified dark flows, due to the fact that the study region is covered with a CO_2 ice cover, and that CO_2 sublimation starts most likely at times when dark flows were observed. Using CRISM spectral data, we detected a CO_2 ice cover of our study region. We found a CO_2 ice band strength of about 0.45 (see Figs. 9 and 11), implying mean pathlengths within transparent CO_2 ice on the order of a few cm (Langevin et al., 2007). If we assume a translucent slab ice cover (not completely transparent) with inclusions of H_2O ice and dust into the CO_2 ice layer, a thickness of this layer of a couple of tens of centimeters is likely. An indication for translucent ice in the region is the occurrence of dark spots on the large dark dune within the polar pit. As described in the introduction, dark spots are suggested to be formed by sublimation of CO_2 ice beneath a translucent slab ice cover and the subsequent degassing through cracks within the slab ice cover (e.g., Piqueux et al., 2003; Kieffer et al., 2006). Diniega et al. (2010, 2013) observed linear gully activity in Russell crater, but presented an alternative formation process involving CO_2 ice. In their hypothesis CO_2 ice blocks break from the top of the dunes due to destabilization processes caused by sublimation in spring and move downslope the dune. During the downward movement the CO_2 ice blocks carve out the levèed linear gullies (Diniega et al., 2013). However, this activity occurred at higher temperatures, results in different gully morphologies, and thus is unlikely to be a plausible origin of the observed gully activity in our study region.

Gardin et al. (2010) investigated the Russell crater dune field (54°S) and observed dark spots on the dunes, which led to the formation of dark linear flow features. These dark linear flows, not to be confused with gully activity observed by Diniega et al. (2010, 2013) and Reiss et al. (2010), have different morphologies and an earlier seasonal formation, by avalanches of mixtures of sand, dust, and sublimating CO_2 ice (Gardin et al., 2010). The dark linear flow features follow the morphology of the dune and are located between aeolian ridge crests, which are similar to the geologic setting in our study region where dark flows also follow the morphology and are located within the gully channel. Furthermore Gardin et al. (2010) measured the seasonal frost cover of the Russel crater dunes with CRISM and described a complete CO_2 frost cover with small amounts of H_2O ice similar to the frost cover found in our study region. Gardin et al. (2010) constrained the timing of the dark flows to the end of winter, while the defrosting of the surface and the formation of dark spots started already in mid-winter. The different timing between the onset of gully activity in Russell crater and our study region is related to the different latitudes at which the two study areas occur. Comparing the observations for dark flows in the more northern latitude of Russell crater (54°S) with those in our study region (68.5°S) nevertheless yields striking similarities, including (1) defrosting of CO_2 surface ice, (2) formation of dark spots, and (3) evolution of dark flows from the dark spots. The dark flows in our study moved material downslope and formed new deposits, which are observable in HiRISE images. Although material was probably transported by dark flows in Russell crater (estimations are 0.25–0.5 m^3 by meter width each year),

direct observations of the moved material, i.e., new deposits, are not available (Gardin et al., 2010).

Hansen et al. (2011, 2012) proposed a formation of dark flows by sublimation of the seasonal CO_2 frost cover. Their investigated dunes with dark flows are in the north polar region and are morphologically similar to dark flows investigated by Gardin et al. (2010) and Kereszturi et al. (2009, 2010, 2011). Hansen et al. (2011, 2012) identified active mass movements on dunes, forming new alcoves and aprons. These features are morphologically different from active linear dune gullies investigated by Diniega et al. (2010, 2013) and Reiss et al. (2010). In particular, the mass wasting features observed by Hansen et al. (2011, 2012) are sand avalanches with typical characteristics such as alcoves and aprons without channels. They are possibly caused by grainflows triggered by spring sublimation of CO_2 frost (Hansen et al., 2011, 2012).

Dundas et al. (2012) reviewed the present-day activity of classical gullies (including the gully presented in our work), dune gullies, and other mass wasting processes in the southern hemisphere on Mars. Their study indicates that the activity of polar pit gullies starts at L_S 159° with the formation of dark spots within gully channels, which often have their origins at boulders (Dundas et al., 2012). In our gully, a link between boulders and dark spots could not be observed. According to our investigation, activity of dark spots in the form of small dark flows down the gully channel slopes and channel starts at L_S ~183°, the same time as in Dundas et al. (2012). Although Dundas et al. (2012) identified some other gullies with dark flows within polar pits, only one gully shows new deposits at its terminus. Dundas et al. (2012) observed an infill of the gully channel between L_S 218° and 249°, which could be further constrained in our study to occur between L_S 218° and 226°. Although the details of the formation process of the dark spots with subsequent dark flows remain unclear in Dundas et al. (2012), a process controlled by the presence or removal of CO_2 frost deposits was deemed to be the most likely scenario.

Investigating the gullies in our study region with spectral data, we found that the gully with the dark flows is unique in that it has weaker band strengths of CO_2 ice and H_2O ice compared to surrounding gullies. Here, the non-icy material of the dark flows lowers the band strengths of CO_2 and H_2O ices. Other gullies show no dark flows, have the same band strengths as their surroundings, and (in spectral image data) cannot be distinguished from their surroundings. If one assumes that the observed dark flows in our study region were formed only by CO_2 gas supported (lubricated) flows, the occurrence of only one single active gully is unlikely. Slope angles (mean slope angles of ~15°), profiles, and morphologies of all gullies on the equator-facing slope are similar within narrow limits. Therefore, we would expect activity due to CO_2 gas supported flows within all gullies, however, this has not been detected.

5.3. Dry flows

Dry flows could be an alternative scenario to form dark flows within the gully in our study region. As seen in the HiRISE images, small dark flows formed in early martian spring at the slopes of the gully channel and the alcove. The small dark flows accumulated within the gully channel and formed large dark flows throughout the entire gully channel. However, as with the CO_2 gas supported flows, activity in only one gully is difficult to explain. One explanation could be that the surface material of the channel slopes and alcove differs from the surrounding gullies, i.e., that the gully alcove and channel comprises outcrops of interbedded layers of sand material. Notice that this is only an assumption and, based on available multi-temporal image and spectral data, we cannot verify that sand material has been eroded from the outcrops. Sublimation of the CO_2 slab ice cover and the resulting destabilization of the slope material could mobilize the sand material, which leads to an accumulation of material in the interior of the gully and the large dark flow could be triggered when a critical mass of sand material is reached. Cedillo-Flores et al. (2011) proposed that sand absorbs ~90% of the solar heat due to low albedo, and conducts it to the underlying CO_2 frost, resulting in sublimation of the underlying frost. This mechanism of sublimation of CO_2 ice beneath the sand layer within the gully channel could support the large flow through the entire gully.

However, the composition and grain size of the dark flows cannot directly be identified via spectral or thermal investigations. The areas with new deposited material are small (resulting in subpixel mixing with the surroundings) and mixing with volatiles hides the spectral properties of the material in the near-infrared. Summer images without the influence of volatiles are not available for the exact location of the gully channel.

As mentioned before, spectral measurements show that the CO_2 and H_2O ice band strengths within the dark flows are weaker than the band strengths of the surroundings, but are still present. The dark flows have a width of ~5–8 m within the gully channel and between ~5 and ~20 m on the apron. CRISM measurements have a resolution of 18 m/pxl, thus measurements of only the dark flow are impossible and the spectral signals from frosted regions surrounding the dark flow are unfortunately incorporated into the measurement. Moreover, as seen in HiRISE images, dark flows are not completely homogeneous and there are some small ice patches within the dark flow areas. As a consequence, spectral signatures of dark material and ices are mixed within CRISM pixels, and we do not know whether the dark material is completely free of ice or not. However, these spectral signatures clearly demonstrate that the dark flows contain at least an ice-free component, if it is not totally ice-free. Thus, the spectral signatures of the dark flows result from a subpixel mixing between the spectral signature of the dark material and the CO_2 ice spectral signature. Two different scenarios would produce similar spectral signatures due to subpixel mixing: (i) spatial mixing between completely defrosted terrain and ice-covered terrain at a scale lower than the pixel size (Fig. 12a), or (ii) spatial mixing between a translucent CO_2 ice layer covered by optically thick dark material (Fig. 12b).

The first scenario requires the presence within CRISM pixels of completely ice-free and thus warm surfaces adjacent to icy surfaces that remain stable over a wide range of L_S, which seems implausible if we expect a translucent CO_2 ice layer to be tens of cm thick. As a consequence, thin regolith flows (optically thick) on top of the CO_2 ice layer seem more likely.

Our investigations (e.g., thin regolith flows on top of CO_2 ice, non-homogeneity of the dark flows, possible sublimation of CO_2 frost superposed by thin dark regolith flows) lead us to the conclusion that the accumulation of sand material at the onset of spring (maybe derived from possible outcrops of interbedded layers of sand material at the alcove and the gully channel slope) within the gully channel and ongoing sublimation of underlying CO_2 slab ice is the most plausible scenario for the observed gully modification. Thus, we prefer a mixture of scenario 2 (CO_2 gas supported flows) with scenario 3 (dry flows).

6. Conclusions

We have gathered seasonal morphological, morphometric, thermal, and near-infrared spectral observations to decipher the seasonal present-day activity of a gully within a south polar pit at 1.44°E and 68.54°S. On the basis of our observations we conclude:

(1) HiRISE albedo images show an early darkening of the surface between L_S ~199° and ~209° within the gully alcove and channel. New deposits on the apron and at the terminus of the gully channel were identified in spring (between

L_S ~218° and ~226°) and can be linked directly to dark flows that occurred within the gully channel. In MY 31 about 300–600 m^3 of material were deposited.

(2) At the onset of spring, near-infrared CRISM images show weaker band strengths of CO_2 ice and H_2O ice within the gully, which implies either smaller amounts of surface ice within the gully or a superposition of sediments on top of the surface ice within the gully. Spectral observations imply that dark material (regolith) covers a translucent slab of CO_2 ice (CO_2 ice contaminated by minor amounts of H_2O ice and dust). This dark material flows through the gully during ongoing sublimation of CO_2 ice and is deposited onto the gully apron. Spectral modeling shows that within a CRISM pixel (<18 m/pxl), the dark flow is characterized by subpixel mixing of covered and exposed icy surfaces. Estimates show areal percentages of a given CRISM pixel between ~31–36% regolith cover and ~64–69% exposed icy surfaces within the observed present-day activity of the dark flow in MY 28 and 29.

(3) The temporal occurrence of morphologic changes of the gully linked to the maximum surface temperatures and to the seasonal behavior of volatiles compared to surrounding gullies implies that mass wasting is most likely related to dry flows and CO_2 frost sublimation. The material of the dry flows (sand) could possibly be mobilized at the slopes of the gully channel and alcove during the sublimation process of the CO_2 ice cover. Furthermore, ongoing sublimation of CO_2 ice within the gully channel could support the mobilization of the dry material (observed dark flows) in the interior of the gully channel. Mobilization of material by liquid H_2O mass wasting processes can be excluded due to low surface temperatures at the onset of spring (~160 K to ~180 K).

Acknowledgments

This research was supported by the Helmholtz Association Germany through the research alliance "Planetary Evolution and Life". We would like to thank two anonymous reviewers for very helpful comments. We acknowledge J.-P. Bibring (Institut d'Astrophysique Spatiale, France) and the European Space Agency for the use of OMEGA data, as well as the CRISM engineering and scientific teams. Furthermore, we would like thank the HiRISE, CTX, TES, and THEMIS teams for providing the great datasets.

References

Appel, M., Ramstad, R., Brown, A.J., McKay, C.P., Fredriksson, S., 2010. Potential model for dark albedo features in the martian polar region observed at 81°N 156°E. Lunar Planet. Sci. XLI. Abstract 1562.

Appéré, T. et al., 2011. Winter and spring evolution of northern seasonal deposits on Mars from OMEGA on Mars Express. J. Geophys. Res. 116, E05001. http://dx.doi.org/10.1029/2010JE003762.

Aston, A.H., Conway, S.J., Balme, M.R., 2011. Identifying martian gully evolution. In: Balme, M.R., Bargery, A.S., Gallagher, C.J., Gupta, S. (Eds.), Martian Geomorphology, Geological Society, vol. 356. Special Publications, London, pp. 151–169.

Balme, M. et al., 2006. Orientation and distribution of recent gullies in the southern hemisphere of Mars: Observations from High Resolution Stereo Camera/Mars Express (HRSC/MEX) and Mars Orbiter Camera/Mars Global Surveyor (MOC/MGS) data. J. Geophys. Res. 111, E05001. http://dx.doi.org/10.1029/2005JE002607.

Bibring, J.-P. et al., 2004a. Perennial water ice identified in the south polar cap of Mars. Nature 428, 327–630.

Bibring, J.-P. et al., 2004b. OMEGA: Observatoire pour la Minéralogie, l'Eau, les Glaces et l'Activité. In: Wilson, A. (Ed.), Mars Express: The Scientific Payload. Eur. Space Agency Spec. Publ., ESA-1240, pp. 37–49.

Bibring, J.-P. et al., 2005. Mars surface diversity as revealed by the OMEGA/Mars Express observations. Science 307, 1576–1581.

Brown, A.J., Byrne, S., Tornabene, L.L., Roush, T., 2008. Louth crater: Evolution of a layered water ice mound. Icarus 196, 433–445.

Brown, A.J., Calvin, W.M., McGuire, P.C., Murchie, S.L., 2010. Compact Reconnaissance Imaging Spectrometer for Mars (CRISM) south polar mapping: First Mars year of observations. J. Geophys. Res. 115, E00D13. http://dx.doi.org/10.1029/2009JE003333.

Brown, A.J., Calvin, W.M., Murchie, S.L., 2012. Compact Reconnaissance Imaging Spectrometer for Mars (CRISM) north polar springtime recession mapping: First 3 Mars years of observation. J. Geophys. Res. 117, E00J20. http://dx.doi.org/10.1029/2012JE004113.

Cantor, B., Malin, M., Edgett, K.S., 2002. Multiyear Mars Orbiter Camera (MOC) observations of repeated martian weather phenomena during the northern summer season. J. Geophys. Res. 107 (E3), 5014. http://dx.doi.org/10.1029/2001JE001588.

Carrozzo, F.G., Bellucci, G., Altieri, F., D'Aversa, E., Bibring, J.-P., 2009. Mapping of water frost and ice at low latitudes on Mars. Icarus 203, 406–420.

Cedillo-Flores, Y., Treiman, A.H., Lasue, J., Clifford, S.M., 2011. CO_2 gas fluidization in the initiation and formation of martian polar gullies. Geophys. Res. Lett. 38, L21202. http://dx.doi.org/10.1029/2011GL049403.

Christensen, P.R., 2003. Formation of recent martian gullies through melting of extensive water-rich snow deposits. Nature 422, 45–48.

Christensen, P.R. et al., 1998. Results from the Mars Global Surveyor Thermal Emission Spectrometer. Science 279, 1692–1698.

Christensen, P.R. et al., 2001. Mars Global Surveyor Thermal Emission Spectrometer experiment: Investigation description and surface science results. J. Geophys. Res. 106 (E10), 23823–23872.

Christensen, P.R. et al., 2004. The Thermal Emission Imaging System (THEMIS) for the Mars 2001 Odyssey Mission. Space Sci. Rev. 110, 85–130.

Clancy, R.T. et al., 2000. An intercomparison of ground-based millimeter, MGS TES, and Viking atmospheric temperature measurements: Seasonal and interannual variability of temperatures and dust loading in the global Mars atmosphere. J. Geophys. Res. 105 (E4), 9553–9571.

Conway, S.J., Lamb, M.P., Balme, M.R., Towner, M.C., Murray, J.B., 2011. Enhanced runout and erosion by overland flow at low pressure and sub-freezing conditions: Experiments and application to Mars. Icarus 211, 443–457.

Costard, F., Forget, F., Mangold, N., Peulvast, J.P., 2002. Formation of recent martian debris flows by melting of near-surface ground ice at high obliquity. Science 295, 110–113.

Dickson, J.L., Head, J.W., 2009. The formation and evolution of youthful gullies on Mars: Gullies as the late-stage phase of Mars' most recent ice age. Icarus 204, 63–86.

Diniega, S., Bryne, S., Bridges, N.T., Dundas, C.M., McEwen, A.S., 2010. Seasonality of present-day martian dune-gully activity. Geology 38, 1047–1050.

Diniega, S., Hansen, C.J., McElwaine, J.N., Hugenholtz, C.H., Dundas, C.M., McEwen, A.S., Bourke, M.C., 2013. A new dry hypothesis for the formation of martian linear gullies. Icarus 225, 526–537.

Dundas, C.M., McEwen, A.S., Diniega, S., Byrne, S., Martinez-Alonso, S., 2010. New and recent gully activity on Mars as seen by HiRISE. Geophys. Res. Lett. 37, L07202. http://dx.doi.org/10.1029/2009GL041351.

Dundas, C.M., Diniega, S., Hansen, C.J., Byrne, S., McEwen, A.S., 2012. Seasonal activity and morphological changes in martian gullies. Icarus 220, 124–143.

Farmer, C.B., Doms, P.E., 1979. Global and seasonal variation of water vapour on Mars and the implication for permafrost. J. Geophys. Res. 84 (B6), 2881–2888.

Forget, F. et al., 2007. Remote sensing of surface pressure on Mars with the Mars Express/OMEGA spectrometer: 1. Retrieval method. J. Geophys. Res. 112, E08S15. http://dx.doi.org/10.1029/2006JE002871.

Gardin, E., Allemand, P., Quantin, C., Thollot, P., 2010. Defrosting, dark flow features, and dune activity on Mars: Example in Russel crater. J. Geophys. Res. 115, E06016. http://dx.doi.org/10.1029/2009JE003515.

Ghatan, G.J., Head, J.W., 2002a. Candidate subglacial volcanoes in the south polar region of Mars: Morphology, morphometry, and eruption conditions. J. Geophys. Res. 107. http://dx.doi.org/10.1029/2001JE001519.

Ghatan, G.J., Head, J.W., 2002b. Cavi Sisyphi, Mars: Nature, origin and initial mapping with MOLA data. Microsymposium 36, MS024.

Hansen, C.J. et al., 2011. Seasonal erosion and restoration of Mars' northern polar dunes. Science 311, 575–578.

Hansen, C.J., Byrne, S., Portyankina, G., Bouke, M., Dundas, C., McEwen, A., Mellon, M., Pommerol, A., Thomas, N., 2012. Observations of the northern seasonal polar cap on Mars: I. Spring sublimation activity and processes. Icarus 225, 881–897.

Head, J.W., Mustard, J.F., Kreslavsky, M.A., Milliken, R.E., Marchant, D.R., 2003. Recent ice ages on Mars. Nature 426, 797–802.

Head, J.W., Marchant, D.R., Kreslavsky, M.A., 2008. Formation of gullies on Mars: Link to recent climate history and insolation microenvironments implicate surface water flow origin. Proc. Natl. Acad. Sci. USA. http://dx.doi.org/10.1073/pnas.0803760105.

Heldmann, J.L., Mellon, M.T., 2004. Observations of martian gullies and constraints on potential formation mechanisms. Icarus 168, 285–304.

Heldmann, J.L., Carlsson, E., Johansson, H., Mellon, M.T., Toon, O.B., 2007. Observations of martian gullies and constraints on potential formation mechanisms II. The northern hemisphere. Icarus 188, 324–344.

Heldmann, J.L., Conley, C.A., Brown, A.J., Fletcher, L., Bishop, J.L., McKay, C.P., 2010. Possible liquid water origin for Atacama Desert mudflow and recent gully deposits on Mars. Icarus 206, 685–690.

Hoffman, N., 2002. Active polar gullies on Mars and the role of carbon dioxide. Astrobiology 2, 313–323.

Hugenholtz, C.H., 2008. Frosted granular flow: A new hypothesis for mass wasting in martian gullies. Icarus 197, 65–72.

Jakosky, B.M., Haberle, R.M., 1992. The seasonal behavior of water in Mars. In: Kieffer, H.H., Jakosky, B.M., Snyder, C.W., Matthews, M.S. (Eds.), Mars. University of Arizona Press, Tucson, pp. 969–1016.
James, P.B., Kieffer, H.H., Paige, D.A., 1992. The seasonal cycle of carbon dioxide on Mars. In: Kieffer, H.H., Jakosky, B.M., Snyder, C.W., Matthews, M.S. (Eds.), Mars. University of Arizona Press, Tucson, pp. 934–968.
Jouannic, G. et al., 2012. Morphological and mechanical characterization of gullies in a periglacial environment: The case of the Russell crater dune (Mars). Planet. Space Sci. 71, 38–54.
Kereszturi, A., Möhlmann, D., Berczi, Sz., Ganti, T., Kuti, A., Sik, A., Horvath, A., 2009. Recent rheologic processes on dark polar dunes of Mars: Driven by interfacial water? Icarus 201, 492–503.
Kereszturi, A., Möhlmann, D., Berczi, Sz., Ganti, T., Horvath, A., Kuti, A., Sik, A., Szathmary, E., 2010. Indications of brine related local seepage phenomena on the northern hemisphere of Mars. Icarus 207, 149–164.
Kereszturi, A., Vincendon, M., Schmidt, F., 2011. Water ice in the dark dune spots of Richardson crater on Mars. Planet. Space Sci. 59, 26–42.
Kieffer, H.H., Chase Jr., S.C., Martin, T.Z., Miner, E.D., Palluconi, F.D., 1976. Martian North Pole summer temperatures: Dirty water ice. Science 194, 1341–1344.
Kieffer, H.H., Christensen, P.R., Titus, T.N., 2006. CO_2 jets formed by sublimation beneath translucent slab ice in Mars' seasonal south polar cap. Nature 772, 793–796.
Kneissl, T., Reiss, D., van Gasselt, S., Neukum, G., 2010. Distribution and orientation of northern-hemisphere gullies on Mars from the evaluation of HRSC and MOC-NA data. Earth Planet. Sci. Lett. 294, 357–367.
Kolb, J.K., Pelletier, J.D., McEwen, A.S., 2010. Modeling the formation of bright slope deposits associated with gullies in Hale Crater, Mars: Implications for recent liquid water. Icarus 205, 113–137.
Kuhn, W.R., Atreya, S.K., 1979. Solar radiation incident on the martian surface. J. Mol. Evol. 14, 57–64.
Langevin, Y. et al., 2007. Observations of the south seasonal cap of Mars during recession in 2004–2006 by the OMEGA visible/near-infrared imaging spectrometer on board Mars Express. J. Geophys. Res. 112, E08S12. http://dx.doi.org/10.1029/2006JE002841.
Langevin, Y. et al., 2010. Inter-Annual Variability of Mars Polar Processes as Observed by OMEGA/Mars Express. Geophysical Research Abstracts, vol. 12, EGU2010-10984-2.
Levine, J.S., Kraemer, D.R., Kuhn, W.R., 1977. Solar radiation incident on Mars and the outer planets: Latitudinal, seasonal, and atmospheric effects. Icarus 31, 136–145.
Malin, M.C., Edgett, K.S., 2000. Evidence for recent groundwater seepage and surface runoff on Mars. Science 288, 2330–2335.
Malin, M.C., Edgett, K.S., Posiolova, L.V., McColley, S.M., Dobrea, E.Z.N., 2006. Present-day impact cratering rate and contemporary gully activity on Mars. Science 314, 1573–1577.
Malin, M.C. et al., 2007. Context camera investigation on board the Mars Reconnaissance Orbiter. J. Geophys. Res. 112, E05S04. http://dx.doi.org/10.1029/2006JE002808.
McEwen, A.S. et al., 2007. Mars Reconnaissance Orbiter's High Resolution Imaging Science Experiment (HiRISE). J. Geophys. Res. 112, E05S02. http://dx.doi.org/10.1029/2005JE002605.
McGuire, P.C. et al., 2009. An improvement to the volcano-scan algorithm for atmospheric correction of CRISM and OMEGA spectral data. Planet. Space Sci. 57, 809–815.
Mellon, M.T., Jakosky, B.M., Kieffer, H.H., Christensen, P.R., 2000. High-resolution thermal inertia mapping from the Mars Global Surveyor Thermal Emission Spectrometer. Icarus 148, 437–455.
Milliken, R.E., Mustard, J.F., Goldsby, D.L., 2003. Viscous flow features on the surface of Mars: Observations from high-resolution Mars Orbiter Camera (MOC) images. J. Geophys. Res. 108 (E6), 5057. http://dx.doi.org/10.1029/2002JE002005.
Möhlmann, D.T.F., 2011. Latitudinal distribution of temporary liquid cryobrines on Mars. Icarus 214, 236–239.
Murchie, S. et al., 2007. Compact Reconnaissance Imaging Spectrometer for Mars (CRISM) on Mars Reconnaissance Orbiter (MRO). J. Geophys. Res. 112, E05S03. http://dx.doi.org/10.1029/2006JE002682.
Musselwhite, D.S., Swindle, T.D., Lunine, J.I., 2001. Liquid CO_2 breakout and the formation of recent small gullies on Mars. Geophys. Res. Lett. 28 (7), 1283–1285.
Pelkey, S.M. et al., 2007. CRISM multispectral summary products: Parameterizing mineral diversity on Mars from reflectance. J. Geophys. Res. 112, E08S14. http://dx.doi.org/10.1029/2006JE002831.
Pelletier, J., Kolb, K., McEwen, A.S., Kirk, R., 2008. Recent gully deposits on Mars: Wet or dry flows? Geology 36, 211–214.
Piqueux, S., Byrne, S., Richardson, M.I., 2003. Sublimation of Mars's southern seasonal CO_2 ice cap and the formation of spiders. J. Geophys. Res. 108 (E8), 5084. http://dx.doi.org/10.1029/2002JE002007.
Raack, J., Reiss, D., Hiesinger, H., 2012a. Gullies and their relationships to the dust–ice mantle in the northwestern Argyre Basin, Mars. Icarus 219, 129–141.
Raack, J., Reiss, D., Ruesch, O., Hiesinger, H., 2012b. Present day activity of south polar gullies on Mars. Lunar Planet. Sci. XLIII. Abstract 1801.
Reiss, D., van Gasselt, S., Neukum, G., Jaumann, R., 2004. Absolute dune ages and implications for the time of formation of gullies in Nirgal Vallis, Mars. J. Geophys. Res. 109, E06007. http://dx.doi.org/10.1029/2004JE002251.
Reiss, D., Hiesinger, H., Hauber, E., Gwinner, K., 2009. Regional differences in gully occurrence on Mars: A comparison between the Hale and Bond craters. Planet. Space Sci. 57, 958–974.
Reiss, D., Erkeling, G., Bauch, K.E., Hiesinger, H., 2010. Evidence for present day gully activity on the Russell crater dune field, Mars. Geophys. Res. Lett. 37, L06203. http://dx.doi.org/10.1029/2009GL042192.
Schmidt, F. et al., 2010. Sublimation of the martian CO_2 seasonal south polar cap. Planet. Space Sci. 58, 1129–1138.
Schon, S.C., Head, J.W., Fasset, C.I., 2009. Unique chronostratigraphic marker in depositional fan stratigraphy on Mars: Evidence for ca. 1.25 Ma gully activity and surficial meltwater origin. Geology 37, 207–210.
Schorghofer, N., Aharonson, O., 2005. Stability and exchange of subsurface ice on Mars. J. Geophys. Res. 110, E05003. http://dx.doi.org/10.1029/2004JE002350.
Shinbrot, T., Doung, N.-H., Kwan, L., Alvarez, M.M., 2004. Dry granular flows can generate surface features resembling those seen in Martian gullies. Proc. Natl. Acad. Sci. USA 101, 8542–8546.
Steward, S.T., Nimmo, F., 2002. Surface runoff features on Mars: Testing the carbon dioxide formation hypothesis. J. Geophys. Res. 107 (E9), 5069. http://dx.doi.org/10.1029/2000JE001465.
Titus, T.N., Kieffer, H.H., 2002. A comparison of the Mars south polar recession rates between 1999 and 2001. Lunar Planet. Sci. XXXIII. Abstract 2071.
Treiman, A.H., 2003. Geologic setting of martian gullies: Implications for their origins. J. Geophys. Res. 108 (E4), 8031. http://dx.doi.org/10.1029/2002JE001900.
Vincendon, M., Langevin, Y., Poulet, F., Bibring, J.-P., Gondet, B., 2007. Recovery of surface reflectance spectra and evaluation of the optical depth of aerosols in the near-IR using a Monte Carlo approach: Application to the OMEGA observations of high-latitude regions of Mars. J. Geophys. Res. 112, E08S13. http://dx.doi.org/10.1029/2006JE002845.
Vincendon, M., Forget, F., Mustard, J., 2010a. Water ice at low to midlatitudes on Mars. J. Geophys. Res. 115, E10001. http://dx.doi.org/10.1029/2010JE003584.
Vincendon, M. et al., 2010b. Near-tropical subsurface ice on Mars. Geophys. Res. Lett. 37, L01202. http://dx.doi.org/10.1029/2009GL041426.
Zuber, M.T. et al., 1992. The Mars Observer laser altimeter investigation. J. Geophys. Res. 97 (E5), 7781–7797.